

1 **YlaN is an iron(II) binding protein that functions to relieve Fur-mediated**
2 **repression of gene expression in *Staphylococcus aureus*.**

3
4 Jeffrey M. Boyd^{1*}, Karla Esquilín-Lebrón¹, Courtney J. Campbell², Kylie Ryan Kaler¹,
5 Javiera Norambuena¹, Mary E. Foley¹, Timothy G. Stephens¹, Gustavo Rios¹, Gautam
6 Mereddy³, Vincent Zheng¹, Hannah Bovermann¹, Jisun Kim⁴, Arkadiusz W. Kulczyk^{1,9},
7 Jason H. Yang³, Todd M. Greco⁵, Ileana M. Cristea⁵, Valerie J. Carabetta⁶, William N.
8 Beavers⁷, Debasish Bhattacharya¹, Eric P. Skaar⁷, Dane Parker⁴, Ronan K. Carroll⁸,
9 Timothy L. Stemmler^{2*}

10
11 ¹Department of Biochemistry and Microbiology, Rutgers, the State University of New
12 Jersey, New Brunswick, NJ, USA.

13 ²Department of Pharmaceutical Sciences, Wayne State University, Detroit, MI, USA.

14 ³Department of Microbiology, Biochemistry, and Molecular Genetics, Center for
15 Emerging Pathogens, Rutgers New Jersey Medical School, Newark, New Jersey, USA

16 ⁴Department of Pathology, Immunology and Laboratory Medicine, Center for Immunity
17 and Inflammation, Rutgers New Jersey Medical School, Newark, New Jersey, USA.

18 ⁵Department of Molecular Biology, Princeton University, Washington Road, Princeton,
19 NJ, USA

20 ⁶Department of Biomedical Sciences, Cooper Medical School of Rowan University,
21 Camden, NJ, USA.

22 ⁷Department of Pathology, Microbiology, and Immunology, Vanderbilt University
23 Medical Center, Nashville, TN, USA.

24 ⁸Department of Biological Sciences, Ohio University, Athens, OH, USA

25 ⁹Institute for Quantitative Biomedicine, Rutgers University, 174 Frelinghuysen Road,
26 Piscataway, NJ 08854, USA.

27
28
29
30
31 ^{\$}Present address: Department of Pathobiological Sciences, Louisiana State University,
32 Baton Rouge, Louisiana, USA.

33 *To whom correspondence may be addressed:

34 Jeffrey M. Boyd, Department of Biochemistry and Microbiology, Rutgers University, 76
35 Lipman Drive, New Brunswick, New Jersey, 08901, Telephone: (848) 932-5604, E-mail:
36 jeffboyd@SEBS.rutgers.edu.

37
38 Timothy L. Stemmler, Department of Pharmaceutical Sciences, Wayne State University,
39 259 Mack Avenue, Detroit, Michigan, 48201, Telephone: (313) 577-5712, E-mail:
40 tstemmle@med.wayne.edu.

41
42 Running Title: YlaN regulates iron homeostasis.

43
44 Keywords: iron, sulfur, Fur, *Staphylococcus aureus*, YlaN

45
46

47 **Abstract**

48 Iron (Fe) is a trace nutrient required by nearly all organisms. As a result of the demand
49 for Fe and the toxicity of non-chelated cytosolic ionic Fe, regulatory systems have
50 evolved to tightly balance Fe acquisition and usage while limiting overload. In most
51 bacteria, including the mammalian pathogen *Staphylococcus aureus*, the ferric uptake
52 regulator (Fur) is the primary transcriptional regulator that controls the transcription of
53 genes that code for Fe uptake and utilization proteins. YlaN was demonstrated to be
54 essential in *Bacillus subtilis* unless excess Fe is added to the growth medium,
55 suggesting a role in Fe homeostasis. Here, we demonstrate that YlaN is expendable in
56 *S. aureus*; however, YlaN became essential upon Fe deprivation. A null *fur* allele
57 bypassed the essentiality of YlaN. The transcriptional response of Fur derepression
58 resulted in a reprogramming of metabolism to prioritize fermentative growth over
59 respiratory growth. The absence of YlaN diminished the derepression of Fur-dependent
60 transcription during Fe limitation. Bioinformatic analyses suggest that *yln* was recruited
61 to Gram positive bacteria and once acquired was maintained in the genome as it co-
62 evolved with Fur. Consistent with a role for YlaN in influencing Fur-dependent
63 regulation, YlaN and Fur interacted *in vivo*. YlaN bound Fe(II) *in vitro* using oxygen or
64 nitrogen ligands with an association constant that is consistent with a physiological role
65 in Fe sensing and/or buffering. These findings have led to a model wherein YlaN is an
66 Fe(II) binding protein that influences Fur-dependent regulation through direct
67 interaction.

68

69 **Importance**

70 Iron (Fe) is an essential nutrient for nearly all organisms. If Fe homeostasis is not
71 maintained, Fe can accumulate in the cytosol where it is toxic. Questions remain about
72 how cells efficiently balance Fe uptake and usage to prevent imbalance. Iron uptake
73 and proper metalation of proteins are essential processes in the mammalian bacterial
74 pathogen *Staphylococcus aureus*. Understanding the gene products involved in Fe ion
75 regulation, uptake, and usage, as well as the physiological adaptations that *S. aureus*
76 uses to survive in Fe-depleted conditions, will provide insight into the role that Fe has in
77 pathogenesis. These data will also provide insight into the selective pressures imparted
78 by the mammalian host.

79

80 **Introduction**

81 Iron (Fe) is an essential nutrient for nearly all organisms. Cytosolic Fe overload
82 can cause toxicity through Fenton chemistry and/or the mismetalation of proteins (1).
83 Because of this paradox, organisms must properly balance Fe uptake with Fe usage to
84 ensure fitness and survival. *Staphylococcus aureus* requires Fe to proliferate and infect
85 host tissues (2). The *S. aureus* genome codes for numerous Fe acquisition systems
86 including the synthesis of two siderophores and one metallophore (3, 4). *In toto*, thus
87 far, 2% of protein coding ORFs code for Fe uptake proteins (3, 5). Once acquired, Fe is
88 used to build iron-sulfur clusters (FeS) and heme, as well as to metalate proteins. The
89 process of building FeS clusters is essential, making Fe acquisition vital (6).

90 The ferric uptake regulator (Fur) is a master regulator of Fe uptake in bacteria
91 (7). Few studies have examined the function of Fur in Gram-positive bacteria including
92 phylum Firmicutes, in which *S. aureus* and *Bacillus subtilis* are members (8). In general,
93 the accepted model for Fur regulation is that holo-Fur acts as a transcriptional repressor
94 or activator (9). Fur can bind a variety of divalent metals *in vitro*, but it is thought that
95 Fe(II) acts as the co-repressor *in vivo* (10, 11). Fur binds directly to operators and
96 represses transcription of genes that code for proteins involved in Fe uptake during Fe
97 replete conditions. When the bioavailable concentration of Fe is low, Fur is demetallated
98 and repression is relieved. Fur often also controls the expression of a sRNA (*tsr25* in *S.*
99 *aureus*) that helps to optimize Fe usage (12).

100 The *yln* gene is essential in *Bacillus subtilis* and the essentiality can be
101 bypassed by growth with excess Fe salts, but the function of Yln has not been
102 described (13). Decreased *yln* expression results in phenotypes that mimic decreased
103 expression of *sufCDSUB*, which codes the essential FeS cluster synthesis system.
104 These findings led us to hypothesize that Yln functions in Fe ion homeostasis. In this
105 study, we created a Δyln mutant in *S. aureus* and demonstrate that this mutation is
106 lethal when cells are cultured in low Fe conditions. The growth defects of a Δyln
107 mutant were relieved by null mutations in *fur* or by fermentative growth. We
108 demonstrate that Yln binds to Fe(II) and that Yln functions to relieve repression of
109 Fur regulated genes during Fe limitation. Our findings support a model wherein Yln is
110 an Fe(II) binding protein that influences Fur-dependent regulation through a direct
111 interaction.

112

113

114 **Results**

115

116 **A *S. aureus* $\Delta ylaN$ mutant is defective in Fe ion processing.**

117 We created a $\Delta ylaN::tetM$ mutant in the community acquired methicillin-resistant
118 *S. aureus* (CA-MRSA) isolate USA300_LAC (WT). The growth of the $\Delta ylaN::tetM$ strain
119 was indistinguishable from that of WT in tryptic soy broth (TSB) medium (Figure S1).
120 We also generated a $yLN::Tn$ strain in LAC that also grew similar to the WT in TSB.
121 The metal ion chelators 2,2'-dipyridyl (DIP) and ethylenediamine-*N,N'*-bis(2-
122 hydroxyphenylacetic acid) (EDDHA) have a high affinity for Fe (14, 15). DIP can cross
123 the cell membrane, whereas the larger EDDHA likely does not (16, 17). Figure 1A
124 displays the growth of the WT with the pCM28 (empty vector) or the $\Delta ylaN::tetM$ strain
125 containing either pCM28 or pCM28_yLN on tryptic soy agar (TSA) media with or
126 without DIP or EDDHA. The $\Delta ylaN::tetM$ strain had a growth defect on both Fe-depleted
127 media and the phenotype could be genetically complimented.

128 To ensure that the growth defect was the result of decreased Fe ion availability
129 and not decreased availability of an alternate metal ion, we treated tryptic soy broth
130 (TSB) medium with Chelex-100 and then added back trace metals except Fe. The
131 $\Delta ylaN::tetM$ strain had a growth defect in this medium and the growth defect was
132 alleviated by the addition of Fe salts (Figure 1B). The Fe-dependent growth defect was
133 apparent after approximately five hours of growth when glucose fermentation slowed
134 and respiratory growth, which requires more Fe-dependent enzymes, was initiated (6).

135 The antibiotic streptonigrin, when combined with intracellular non-chelated Fe
136 ions (sometimes referred to as “free Fe”) and electrons, causes double-stranded DNA
137 breaks (18). Strains that are hypo- or hyper-active for Fe uptake are more resistant and
138 more sensitive to streptonigrin, respectively (19). We created TSA overlays containing
139 the WT with pEPSA5 (empty vector) or the $\Delta ylaN::tetM$ strain with pEPSA5 or
140 pEPSA5_yLN. The pEPSA5_yLN vector placed *yLN* under the transcriptional control
141 of *xy/RO* allowing for xylose induction of *yLN* expression. We subsequently spotted
142 streptonigrin and measured the zone of growth inhibition. The $\Delta ylaN::tetM$ strain was
143 more resistant than the WT to growth in the presence of streptonigrin, suggesting that
144 this strain had decreased streptonigrin associated Fe (Figure 1C). Over-production of
145 *yLN* made cells more sensitive to streptonigrin, suggesting that they had increased
146 streptonigrin accessible Fe.

147

148 **Null mutations in *fur* suppress growth defect of the *yLN* mutant in Fe limiting
149 conditions.**

150 We conducted a suppressor screen to investigate *YLN* essentiality under low Fe
151 growth conditions. We individually plated ten independent cultures of the $\Delta ylaN::tetM$
152 strain on TSA medium containing 700 μ M DIP. Colonies arose that contained second
153 site mutations that permitted growth. We mapped these mutations, and nine strains
154 contained a single nucleotide polymorphism (SNP) in the gene that codes for the ferric
155 uptake regulator (Fur) resulting in the following variants: V29F (isolated twice), C103Y
156 (isolated twice), E52X, T62M, R61I, R23H, and E11X (henceforth referred to as *fur**).
157 The tenth strain had a guanine to cytosine transversion mutation in the 5' untranslated
158 region 13 base pairs upstream of the predicted translation start codon.

159 We linked a transposon (Tn) (SAUSA300_1452; *proC*) to the *fur** mutation and
160 then transduced the *fur** allele into the WT and Δ *ylaN*::*tetM* strains by selecting for the
161 *proC*::Tn. As expected, some transductants had the *fur** allele while others retained the
162 WT copy of *fur*. All isolates with *fur** suppressed the growth defect of Δ *ylaN*::*tetM* on
163 TSA medium with DIP, whereas those isolated with the WT *fur* allele did not (Figure
164 2A).

165 Two results are consistent with the hypothesis that the mutant *fur* alleles are null
166 and recessive. First, we found that a Δ *fur*::*tetM* allele could suppress the DIP and
167 EDDHA sensitivity phenotypes of a *ylaN*::Tn mutant (Figure 2A). Second, we were able
168 to genetically complement the *fur** and Δ *fur*::*tetM* alleles (Figure 2B).

169 We tested the hypothesis that the *fur** allele was derepressing transcription of Fe
170 uptake systems, and thereby increasing Fe import. We quantified the total Fe load in the
171 WT and Δ *ylaN*::*tetM* strains after growth in TSB. As expected, there was a significant
172 increase in Fe in the *fur** mutant strains (Figures 2C and S2). The *fur** allele also
173 increased streptonigrin sensitivity of the Δ *ylaN*::*tetM* mutant (Figure 2D). These data are
174 consistent with the hypothesis that the *fur** allele increased the total Fe load and the
175 amount of intracellular non-chelated Fe.

176 We next tested the hypothesis that increased Fe uptake by introduction of the
177 *fur** allele suppressed the DIP sensitivity of the Δ *ylaN* strain. We introduced a *fhuC*::Tn
178 mutation into the Δ *ylaN*::*tetM* *fur** strain, which inactivated the siderophore-dependent
179 Fe uptake systems (20, 21). The *fhuC*::Tn mutant had a growth defect on plates
180 containing DIP as previously reported (Figure S3) (6). The *fur** allele suppressed the
181 growth defect of the Δ *ylaN*::*tetM* *fhuC*::Tn mutant suggesting that the null fur alleles
182 were suppressing the growth defects of the Δ *ylaN* mutant by a mechanism other than
183 promoting Fe uptake.

184 185 **Iron-deprivation or the loss of Fur alters the regulation of central metabolism.**

186 We developed and tested two non-mutually exclusive hypotheses to explain why
187 a null *fur* allele suppressed the essentiality of *YlaN* under low Fe growth conditions: 1.
188 The absence of functional Fur alters metabolism and thereby permits the Δ *ylaN* mutant
189 to grow with a lower Fe allowance; and 2. *YlaN* functions to relieve Fur-dependent
190 repression of transcription under low Fe growth conditions, which is bypassed by a null
191 *fur* mutation.

192 We first tested the hypothesis that a null *fur* allele alters the regulation of
193 metabolism to permit growth with a lower Fe allowance. We examined the effect of Fur
194 and divalent metal starvation on the transcriptome. RNAs were quantified using RNA-
195 sequencing after the WT and Δ *fur*::*tetM* strains were cultured in TSB with and without
196 120 μ M DIP. This concentration of DIP was chosen because it does not cause a
197 substantial defect in growth in either strain under the growth conditions utilized.
198 Principal component analysis (PCA) of the regulons indicated that each strain and
199 growth condition had a unique regulon and the individual regulons clustered (Figure
200 S4). We verified the altered RNA abundances using quantitative PCR (qPCR) (Figure
201 S5 and Table S1).

202 As expected, there was overlap between the WT vs. Δ *fur*::*tetM* and WT vs. WT +
203 DIP regulons (Table S2). These regulons shared \approx 30% of the genes with a \log_2 fold-
204 change in abundance $> \pm 2$ (Figure S6). The cause of the differences between these

205 regulons is likely twofold. First, the addition of DIP competes for divalent metals altering
206 the activity of divalent metal-dependent transcriptional regulators such as MntR and Zur.
207 In support of this idea, there was increased transcription of divalent metal uptake genes
208 (e.g. *abcA*, and *mntABC*) in the DIP regulon that were absent in the Fur regulon (Figure
209 S7). Second, we did not add enough DIP to fully derepress Fur. In support of this, the
210 transcription of Fe uptake genes (e.g. *iruO*, and *sstB*) was not fully derepressed in DIP
211 treated cells (Figure S7).

212 Detailed analyses of the regulons showed that several genes coding nutrient
213 uptake and energy generation enzymes had altered regulation in the $\Delta fur::tetM$ strain
214 and DIP challenged WT (Figure S8). RNAs encoding Fe-uptake (*sbnB*) and Fe-requiring
215 proteins (ribonucleotide reductase: *nrdD*) were increased and decreased, respectively,
216 in the $\Delta fur::tetM$ strain and in the WT upon DIP challenge (Figures 3A and B and Table
217 S2). There was decreased abundances of RNAs that code respiratory complexes
218 (cytochrome oxidase: *qoxD*) and an increase in RNAs coding fermentation enzymes
219 (formate dehydrogenase: *fdh*) in the $\Delta fur::tetM$ strain and in DIP challenged WT
220 (Figures 3A and B and Table S2).

221

222 **Iron-deprivation or the absence of Fur decreases dioxygen respiration.**

223 To test the hypothesis that Fur downregulates cellular respiration in Fe-limiting
224 conditions we quantified O₂ consumption. First, we validated the technique by
225 monitoring O₂ consumption in a *hemB::Tn* mutant which cannot mature cytochrome
226 oxidases (22). The *hemB::Tn* strain had no detectable O₂ consumption verifying that
227 respiration is the primary consumer of O₂ under the growth conditions examined (Figure
228 S9A). We next examined the rates of O₂ consumption using the WT and $\Delta fur::tetM$
229 strains cultured with varying concentration of DIP. The rate of O₂ consumption
230 decreased in the WT as a function of increasing DIP (Figure 3C). The basal rate of O₂
231 consumption was decreased in the $\Delta fur::tetM$ mutant when compared to the WT.
232 Dioxygen consumption was largely unaffected in the $\Delta fur::tetM$ strain when challenged
233 with DIP consistent with the hypothesis that Fur derepression was responsible for the
234 decreased O₂ consumption in the DIP-challenged WT.

235 We further tested the ability of the WT and $\Delta fur::tetM$ strains to generate a
236 membrane potential using the fluorescent dye 3'3'-diethyloxacarbocyanine iodide
237 (DiOC₂). When bacteria generate a membrane potential, DiOC₂ accumulates
238 intracellularly, resulting in a shift from emitting green fluorescence to emitting red
239 fluorescence (23, 24). We validated the technique by analyzing the ability of DiOC₂ to
240 detect altered membrane potential between the WT and *hemB::Tn* strains. Whereas
241 there was a red shift in fluorescence in the WT strain, very little red fluorescence was
242 noted in the *hemB::Tn* mutant, indicative of a reduced membrane potential (Figure
243 S9B). The addition of carbonyl cyanide m-chlorophenyl hydrazone (CCCP), which
244 dissipates the transmembrane electric potential ($\Delta\psi$) and ΔpH , resulted in decreased
245 fluorescence in the WT (Figure S9B). We next examined the membrane potential in the
246 WT and $\Delta fur::tetM$ strains after culture with and without 500 μM DIP. The membrane
247 potential of the WT strain decreased upon co-culture with DIP (Figure 3D). The
248 membrane potential was lower in the $\Delta fur::tetM$ strain compared to the WT. There was
249 little change in the membrane potential in the $\Delta fur::tetM$ strain when co-cultured with

250 DIP consistent with the hypothesis that Fur derepression was responsible for the
251 decreased membrane potential in the WT.

252
253 **Iron-deprivation or the loss of Fur globally alters cellular metabolism.**

254 We performed genome-scale metabolic modeling using our RNA-sequencing
255 data and O₂ consumption measurements as modeling constraints (Table S3) (25).
256 Consistent with these data, modeling analyses predicted decreased NADH
257 dehydrogenase, succinate dehydrogenase, and cytochrome oxidase activity (Figure
258 4A), as well as decreased TCA cycle activity (Figure 4B) in iron limiting conditions. To
259 validate these predictions, we experimentally measured the activity aconitase (AcnA), a
260 TCA cycle FeS cluster requiring enzyme, in the WT $\Delta fur::tetM$ strains co-cultured with
261 DIP (19). AcnA activity was decreased in Fe limiting conditions and nearly undetectable
262 in the $\Delta fur::tetM$ strain (Figure 4C).

263 Modeling analyses further predicted several other global metabolic changes,
264 including increased activity through acetate fermentation (Figure 4D), branched-chain
265 amino acid biosynthesis, nucleotide biosynthesis, and the urea cycle. Modeling
266 analyses also predicted decreased activity in lipid and cell wall biosynthesis and tRNA
267 synthetase pathways (Table S3). Collectively, these data and modeling analyses are
268 consistent with the hypothesis that upon Fe deprivation, Fur-dependent transcriptional
269 repression is relieved, resulting in carbon flux being redirected to decrease reliance
270 upon Fe-dependent enzymes, including respiratory complexes and TCA cycle enzymes,
271 and increasing carbon flux through fermentation pathways to maintain redox
272 homeostasis.

273
274 **Iron-deprivation or the absence of Fur alters metabolite abundances.**

275 To validate some of these modeling predictions, we cultured the WT and
276 $\Delta fur::tetM$ strains, as we did for the transcriptomic experiments, before isolating
277 metabolites and conducting untargeted metabolomic analyses. We also cultured the
278 strains in the absence of O₂ to force fermentation. The DIP treated WT and the
279 $\Delta fur::tetM$ strain shared several metabolites that had altered abundances. For the
280 aerobic samples, the $\Delta fur::tetM$ strain had more significantly altered metabolites than
281 the DIP challenged WT (Tables 1 and S4), whereas the number of significantly altered
282 metabolites were similar in the fermenting strains (Tables 2 and S4).

283 Independent of the presence of O₂, the absence of Fur or the presence of DIP
284 decreased pools of amino acids with nitrogen containing side chains (His, Gln, Pro) and
285 decreased abundances of metabolites associated with nitrogen homeostasis (citrulline,
286 ornithine, argininosuccinate, glutamine, N-acetyl-glutamine). Consistent with model
287 predictions that nucleotide metabolism is induced by iron limitation (Table S3), aerobic
288 co-culture with DIP, or Fur deletion, increased the abundance of adenine, guanine,
289 thymine, and uracil. We hypothesize that this metabolic shift occurs to increase the
290 production of the nitrogen containing metallophore, staphylopine, and the siderophores,
291 staphyloferrin A and B. Consistent with this hypothesis, there were altered abundances
292 of diaminopimelic acid, pyruvate, O-phospho-serine, serine, ornithine and histidine
293 which are metabolic precursors used for the synthesis of these metallophores (5, 23,
294 26).

295 During aerobic growth, the $\Delta fur::tetM$ strain showed an increased accumulation
296 of pyruvate, malate, α -ketoglutarate, and succinate. These metabolites were not altered
297 in the fermenting cells suggesting that flux though the TCA cycle was altered during
298 respiratory growth during Fe limitation.

299

300 **Fermentative growth bypasses the essentiality of YlaN during Fe deprivation.**

301 We tested the hypothesis that a null *fur* mutation alters metabolism and thereby
302 bypasses the essentiality of YlaN in Fe-depleted media. We cultured the parent
303 (*proC::Tn*), and isogenic *fur**, $\Delta ylaN::tetM$, and $\Delta ylaN::tetM fur^*$ strains on solid or in
304 liquid media with or without metal chelator in the presence and absence of O₂. Since no
305 other respiratory substrate was added to the media, anaerobic growth forces
306 fermentation. The $\Delta ylaN::tetM$ strain displayed a growth defect with chelator when
307 cultured aerobically (Figures 5A and C) but not when cultured anaerobically (Figures 5B
308 and D). All four strains grew equally well with chelator when incubated anaerobically.
309 These data are consistent with the hypothesis that the essentiality of YlaN in Fe deplete
310 conditions can be bypassed by fermentative growth.

311

312 **YlaN is required to relieve Fur-dependent repression of transcription.**

313 We tested the second hypothesis that YlaN is required to relieve Fur-dependent
314 repression of transcription under low Fe growth conditions. The *fhuC*, *isdC*, *tsr25*, and
315 *sbnA* genes are regulated by Fur (Table S2 and Figure S10) and have Fur-boxes in
316 their promoters suggesting direct Fur regulation. Consistent with this, *fhuC*, *isdC*, and
317 *tsr25* transcriptional reporters were more active in the $\Delta fur::tetM$ strains. We were
318 unable to transduce the *sbnA* reporter into the *fur* mutant. All four promoters had
319 increased activity in the WT upon growth with DIP (Figures 6A-D). In contrast, none of
320 the promoters responded to DIP in the $\Delta ylaN::tetM$ mutant.

321 We next quantified RNA transcripts corresponding to *isdC*, *fhuD*, *tsr25*, *sbnA*,
322 and *isdA* in the WT and $\Delta ylaN::tetM$ strains after growth with and without DIP. All
323 transcripts increased in the WT strain upon DIP challenge; however, none of these
324 transcripts significantly responded to DIP challenge in the $\Delta ylaN::tetM$ strain (Figures
325 6E-I).

326 We next monitored siderophore production using chrome azurol S (CAS). Fe-
327 bound CAS is blue in color. The addition of siderophores competes with CAS for the Fe
328 resulting in apo-CAS, which is orange. We cultured the parent (*proC::Tn*), $\Delta ylaN::tetM$,
329 *fur**, and $\Delta ylaN::tetM fur^*$ strains in TSB before measuring CAS competition using spent
330 media. The spent media from the strains containing the *fur** mutations were better able
331 to compete for Fe than the parent (Figure 6J). The spent media from the $\Delta ylaN::tetM$
332 strain did not alter the absorbance of the CAS-Fe complex. These data are consistent
333 with the hypothesis that the presence of YlaN functions to relieve Fur-dependent
334 repression of transcription upon Fe limitation, which can be bypassed by a null *fur*
335 mutation.

336

337 **YlaN and Fur likely co-evolved.**

338 We compared the conservation of *ylaN* and *fur* in bacterial genomes. The
339 presence of *ylaN* is restricted to Firmicutes, forming a clear monophyletic clade (Figure
340 7). The Fur sequences from YlaN-positive genomes are paraphyletic, with the

341 sequences from YlaN-negative genomes having diverged early in this group. This
342 suggests that YlaN was lost from these lineages during the early stages of its evolution.
343 There are only six sequences in the tree (all Firmicutes) that are from YlaN-positive
344 genomes but are not part of the monophyletic clade of Firmicutes Fur sequences.
345 These sequences are positioned with non-Fur sequences in the tree (e.g., Zur and
346 PerR) and are likely to be PerR. They were recruited into the tree during the DIAMOND
347 (sequence similarity-based) search, and thus support the singular origin of YlaN in
348 Firmicutes.

349 Comparison of the Firmicutes Fur and YlaN phylogenies (Figure S11 and S12)
350 demonstrates that whereas there is significant discordance between both trees,
351 generally, many of the closely related groups of sequences are present in both trees
352 (represented by the colored lines) and the major differences arise from the early
353 diverging nodes which are weakly supported (i.e., have bootstrap support <95%). This
354 result suggests that Fur and YlaN have been co-evolving, although given the lack of
355 phylogenetic signal for the early diverging nodes in both protein trees, this hypothesis is
356 currently provisional.

357

358 ***Bacillus subtilis* YlaN and Fur and interact *in vivo*.**

359 The findings that the presence of YlaN alters the ability of Fur to respond to Fe
360 limitation and that YlaN and Fur likely co-evolved in the Firmicutes led to the hypothesis
361 that these two proteins physically interact with each other. We performed an
362 immunoaffinity purification-mass spectrometry analysis of YlaN in non-pathogenic *B.*
363 *subtilis*, which like *S. aureus*, is a member of the phylum Firmicutes. We chose to work
364 in *B. subtilis* because the immunopurification protocol conditions are optimized (27) and
365 for safety concerns since the sample preparation can create aerosols. We created a
366 strain encoding an N-terminally fused YFP-YlaN from the *amyE* locus, which was under
367 the transcriptional control of an IPTG-inducible promoter. YFP-YlaN was
368 immunopurified from both logarithmic and stationary phase cells and co-isolated
369 proteins were identified by mass spectrometry. Fur was the most abundant protein co-
370 isolated with YFP-YlaN in both exponential and stationary phase (Table S5). The FeS
371 cluster synthesis machinery (SufCDSUB), FeS cluster assembly factors (SufA and
372 SufT), and Fe-requiring proteins (i.e., GlcF, NarH, QcrA, and CitB) were also identified
373 as interacting partners. These data support the hypothesis that YlaN interacts with Fe
374 utilizing proteins.

375 Using the AlphaFold2 structural models for *S. aureus* YlaN and Fur, we were
376 able to model a potential interaction configuration (Figure S13). In these models, the
377 highly conserved residues of YlaN helix two (EEVLDTQMFG) interact with the DNA
378 binding domain of Fur.

379

380 ***Staphylococcus aureus* YlaN binds Fe(II) with a physiological relevant affinity.**

381 We tested the hypothesis that YlaN binds Fe(II) using a competition assay (28-
382 30). This assay measures Fe(II) binding affinity of a protein under heterogenous
383 solution conditions, which better mimics *in vivo* conditions. We measured changes in
384 the UV-Vis signal at 365 nm from the apo-form of the chelator Mag-Fura-2, which
385 decreases upon Fe(II) loading of the chelator. Binding analyses were completed on two
386 independently prepared protein samples. Data were simulated to deconvolute the

387 protein-metal binding relative to the known chelator metal binding affinity (for Mag-Fura-
388 2, Fe(II) binding $K_d = 6.5 \pm 0.5 \mu\text{M}$). The Fe(II) binding affinity for YlaN was best fit by
389 one independent K_d at $2.07 \pm 0.46 \mu\text{M}$ (Figure 8A).

390

391 **Fe(II) binding to YlaN alters its secondary structure and thermal stability.**

392 We examined the impact of Fe(II) binding on the secondary structure of YlaN
393 using circular dichroism (CD) spectroscopy. Comparison of average CD spectra of the
394 apo- and holo-YlaN show some change between the two protein states (Figure 8B), with
395 similar negative features at both 207 and 223 nm; wavelengths which are attributed to
396 α -helical structures (31). These negative features become more prominent upon Fe(II)
397 binding. Simulation results are shown in Table S6. These results show an overall trend
398 of increasing helical structure coupled with Fe(II) binding. The helical content of Fe(II)
399 loaded protein is slightly increased (from 31% in the apo state to 40% in the holo), while
400 the relative values of the additional structural elements only slightly decrease,
401 suggesting that upon Fe(II) binding, YlaN increases its overall helical structure. Root-
402 mean-square deviations (RMSD) between theoretical and empirical data for both apo-
403 and holo-YlaN CD spectra are consistently low, suggesting simulations accurately
404 predict the secondary structure change for each construct.

405 We examined the thermal stability of apo- and Fe(II) bound YlaN using
406 differential scanning calorimetry (DSC). The apo-protein had a two-phase thermal
407 stability profile (Figure 8C and Table S7). Melting temperatures for apo-YlaN were 72.0
408 and 77.5 °C. Fe(II) binding to YlaN increased the melting temperatures; the lower T_m
409 was increased to 75.3 °C while the higher T_m value was increased to 79.8 °C, indicating
410 that Fe(II) binding increased the protein's thermal stability.

411

412 **The YlaN Fe(II) binding environment consists of only oxygen and/or nitrogen 413 ligands.**

414 We probed the structure and electronic properties of Fe(II)-loaded YlaN to
415 determine bound-metal coordination geometry. Structural details for Fe(II) bound to
416 YlaN were measured using Fe k -edge X-Ray Absorption Spectroscopy (XAS) (32).
417 Normalized X-ray Absorption Near Edge Spectroscopy (XANES) data was used to
418 determine the average metal oxidation state, spin state, and ligand coordination
419 symmetry (28). The XANES edge shape (Figure 9A, left) and first inflection edge energy
420 at around 7123 eV (Table S8) suggest Fe-loaded YlaN contains only Fe(II). The pre-
421 edge feature (Figure 9A, right) between 7110-7115 eV represents the Fe(II) 1s-3d
422 electron transition. The area under the curve (Table S8) indicates protein bound Fe(II) is
423 held in a highly symmetric 6-coordinate metal ligand environment.

424

425 The strength of XAS is the high accuracy seen in the metal-ligand bond length
426 values obtained by simulating the Extended X-Ray Absorption Fine Structure (EXAFS)
427 portion of the XAS spectrum. In review, simulations of EXAFS data provide metal-ligand
428 bond lengths at an accuracy of $\pm 0.02 \text{ \AA}$, while information regarding metal-ligand
429 coordination numbers are obtained at an accuracy of ± 1.0 and ligand identity narrowed
430 to within one row of the periodic table (32). All Fe data were fit out to a k -space value of
431 12.5 \AA^{-1} to eliminate high energy noise. Calibration from Fe(II) and Fe(III) theoretical
432 model compounds were used for E_0 and Sc parameters. E_0 values for Fe-O, Fe-N, Fe-C
were set at -10 eV and a scale factor of 0.95 was used to fit the data. Figure 9B shows

433 the raw and simulated EXAFS and Fourier Transform (FT) of the EXAFS. Best fit
434 simulations are listed in Table S9, which fit O/N as nearest neighbor ligands, followed
435 by C as long range ligands. These data are consistent with a highly symmetric,
436 octahedral Fe(II) coordination environment consisting of O/N ligands. The presence of C
437 ligand scattering as a long-range interaction indicates Fe(II) in the sample with higher
438 order, consistent with attachment to amino acids, as opposed to being bound
439 adventitiously. Under these parameters, the average Debye Waller Factor and F'
440 values, measures of absorber-scatter bond disorder, and overall simulation
441 convergence between theoretical and empirical data, were highly favorable.
442

443 **Discussion**

444 We initiated this study after data produced by Peters *et al.* suggested that YlaN
445 had a role in Fe ion homeostasis in *B. subtilis*. Unlike *B. subtilis*, YlaN is not essential in
446 *S. aureus* under standard growth conditions. This difference in essentiality may be
447 explained by the metabolic potential of these two organisms. Whereas *S. aureus* is a
448 robust glucose fermenter in standard laboratory media, *B. subtilis* is inefficient at
449 fermenting glucose in the absence of a respiration substrate (33, 34). In general,
450 respiratory growth utilizes more FeS cluster proteins than fermentative growth (35). In
451 support of this, *S. aureus* has decreased transcription of Fe uptake systems and imports
452 less Fe when cultured in conditions that favor fermentative growth over respiratory
453 growth (36). It is likely that *S. aureus* temporarily promotes a fermentative metabolism in
454 low Fe conditions to prioritize the metalation of essential Fe enzymes, while sacrificing
455 the Fe-demanding, but high ATP yielding respiratory growth.

456 We demonstrate that a null *fur* mutation bypasses the need for YlaN under Fe
457 limiting conditions. The reason for this appears to be twofold. First, in the absence of
458 YlaN, Fur does not properly derepress transcription during Fe limitation, which is
459 bypassed by the introduction of a null *fur* allele. Second, in the absence of Fur, cells
460 switch to a fermentative metabolism. Consistent with our findings herein, it was
461 previously demonstrated that growth with DIP, or the absence of Fur, resulted in
462 increased lactate fermentation (37). A second study found that growing with low Fe
463 decreased abundances of metabolites associated with the TCA cycle and increased
464 abundances of fermentation byproducts including acetate and lactate (36). We
465 discovered that forcing fermentative growth by anaerobic incubation decreased the Fe-
466 dependent growth defect of the Δ *ylaN* strain. These data are consistent with a model
467 wherein YlaN functions to relieve Fur-dependent repression of transcription during Fe
468 limitation. In the absence of YlaN, *S. aureus* cannot trigger the Fur-dependent switch to
469 an Fe-restrictive fermentative metabolism resulting in a severe growth defect.

470 Bioinformatic analyses demonstrated that *ylaN* was recruited to a *fur*-containing
471 genome and was then retained long-term, apparently shaping the evolutionary trajectory
472 of *fur*. It is currently unknown if the *S. aureus* Fur binds Fe(II); however, YlaN does bind
473 Fe(II) and the data here support the hypothesis that YlaN functions in Fur-dependent
474 regulation. In support of this, YlaN and Fur interact *in vivo*. Modeling data predict that
475 YlaN binds to Fur at the same location where it binds to DNA. The internal
476 concentration for Fe(II) in *S. aureus* cells is unknown, but it is predicted to be \approx 6 μ M in
477 aerobically cultured *E. coli* (38). YlaN binds Fe(II) with an affinity ($K_D \approx$ 2 μ M) that is
478 consistent with it being holo and apo in Fe replete and deplete conditions, respectively.
479 The Δ *ylaN* mutant has less streptonigrin associated Fe suggesting that it is not
480 functioning solely as an Fe buffer or Fe chaperone. The manuscript by Demann *et al.*,
481 which was co-submitted with this manuscript, demonstrates that the YlaN prevents the
482 DNA binding activity of Fur (39). These data have resulted in a working model (Figure
483 10) wherein during Fe replete conditions, holo-Fur binds to operators of genes utilized in
484 Fe uptake and represses transcription. During Fe limitation, YlaN interacts with Fur,
485 resulting in derepression of Fur-regulated genes, as well as decreased expression of
486 genes coding Fe requiring proteins. The latter is likely indirect regulation possibly
487 requiring the *tsr25* sRNA. Ultimately, this results in the derepression of Fe uptake

488 systems and a reprogramming of central metabolism to compete in a low Fe
489 environment.

490 YlaN also significantly interacted with Fe or FeS cluster-binding proteins. The
491 genomes of *S. aureus* and *B. subtilis* lack the described bacterial Fe(II) binding proteins
492 CyaY and IscX (40, 41), which act as Fe(II) chaperons and have been shown to interact
493 with the Isc FeS cluster biosynthesis machinery (42). Further biochemical tests are
494 required to determine how YlaN promotes Fur derepression and to determine whether
495 YlaN can function as an Fe donor for FeS cluster synthesis or for the maturation of Fe
496 proteins.

497 The findings herein have led to a model where YlaN acts as an Fe(II) chaperone.
498 When the concentration of Fe(II) is sufficient, Fur and YlaN are metalated. Holo-Fur
499 binds to operators to modulate transcription. When Fe is scarce, YlaN competes with
500 Fur for Fe(II), and possibly DNA, resulting in demetallation of Fur and decreased DNA
501 association. This results in derepression of Fe uptake systems and a reprogramming of
502 central metabolism to compete under a low Fe environment.

503

504 **Materials and Methods**

505

506 **Chemicals and growth conditions.**

507 All bacterial strains used in this study (Table 3) were derived from the community
508 associated methicillin-resistant *Staphylococcus aureus* isolate USA300_LAC (43).
509 Bacteria were grown at 37 °C in tryptic soy broth (TSB) (MP Biomedicals) and shaking
510 at 200 rotations per minute. Solid media was generated by adding 1.5% (wt/vol) agar
511 (VWR). Chelex-treated TSB was prepared as previously described (44). Unless stated
512 otherwise, cells were cultured in 10 mL capacity culture tubes containing 1.5 mL of
513 liquid medium. Quantitative growth was conducted using a 96-well plate reader BioTek
514 808E visible absorption spectrophotometer at 37 °C and shaking. For quantitative
515 growth, bacteria strains were grown for 18 hours and washed twice with PBS before
516 diluting them to an optical density at 600 nm (OD₆₀₀) of 0.02 in 200 µL. Anaerobic
517 growth was conducted using a 37 °C incubator inside of a CO₂ anaerobic chamber
518 containing an oxygen scavenging catalyst to maintain oxygen levels <1ppm. Anaerobic
519 growth was quantified by measuring culture OD₆₀₀ after 18 hours.

520 Streptonigrin sensitivity assays were performed as previously described (10).
521 Overnight TSB cultures were washed with PBS and diluted to OD₆₀₀ 0.1. One hundred
522 µL of cell suspension were added to 4 mL of 3.5% TSA. For genetic complementation
523 studies, the TSA top agar also contained 1% xylose and 30 µg mL⁻¹ chloramphenicol
524 (Cm). 5 µL of 2.5 mg mL⁻¹ of streptonigrin diluted in DMSO was spotted atop the top
525 agar overlay. The zone of inhibition was measured after overnight incubation at 37 °C.

526 When necessary, antibiotics were added at the final following concentrations:
527 100 µg mL⁻¹ ampicillin (Amp); 10 µg mL⁻¹ chloramphenicol (Cm); 10 µg mL⁻¹
528 erythromycin (Erm); 3 µg mL⁻¹ tetracycline (Tet). Protein concentrations were
529 determined using Bradford reagent (Bio-Rad Laboratories Inc., Hercules, CA). DNA
530 primers were purchased from IDT and are listed in Table S10. Molecular reagents were
531 purchased from New England Biolabs, unless otherwise stated. Unless stated
532 otherwise, all chemicals were purchased from Sigma-Aldrich (St. Louis, MO). Sanger
533 DNA sequencing was performed at Azenta (South Plainfield, NJ).

534

535 **Plasmid and strain construction.**

536 *Escherichia coli* DH5α was used for plasmid preparation. The restriction minus
537 strain *S. aureus* RN4220 was used for transformation (45) and transductions were
538 carried out using bacteriophage 80α (46).

539 We used the pJB38 plasmid to create the *Δy/aN::tetM* mutant as previously
540 described (47). Briefly, the chromosomal regions upstream and downstream of *y/aN*
541 were amplified by PCR using the following primer pairs: YCCylnupFor and
542 ylnupTetRrev; tetRylnupFor and ylnupTetRrev. We amplified *tetM* from strain
543 JMB1432 using primers ylnupTetRfor and tetRylnupTetRrev. The amplicons were gel
544 purified and combined with pJB38 that had been digested with Sall and Nhel. The
545 fragments were combined using yeast recombinational cloning (48, 49). The
546 pEPSA5_ylnup vector was constructed by amplifying *y/aN* from genomic DNA using the
547 following primer pair: YlnA forEcoRI and YlnA revSall. The pCM28_ylnup vector was
548 made by amplifying *y/aN* from genomic DNA using the following primer pair: YlnA
549 for5BamHI and YlnA revSall. To create the pOS_isdC_gfp transcriptional reporter

550 plasmid we amplified the *isdC* promoter using the following primer pair:
551 pOS_saeP1_gfp with pOS_iscC_hindIII 5. For the pOS_fhuA_gfp transcriptional
552 reporter plasmid we amplified the *fhuA* promoter using the following primer pair:
553 pOS_fhuA_hindIII 5 and pOS_fhuA_kpnI 3. To create the pOS_ts25_gfp transcriptional
554 reporter, we amplified ts25 using the following primer pair: HindIII ts25p up and kpnI
555 ts25p dwn2. For the pOS_sbnA_gfp transcriptional reporter plasmid we amplified the
556 *sbnA* promoter using the following primer pair: Sbn pro3 kpnI and Sbn pro5 hindIII. To
557 create the pGEX-6P-1_yaN expression vector we amplified *ylan* from *S. aureus* using
558 the following primer pair: ylan5GSTBamHI and ylan3Xhol. The amplicon was digested
559 with BamHI and Xhol and ligated into similarly digested pGEX-6P-1. All plasmids were
560 sequence verified.

561 To construct the *B. subtilis* *yfp-ylan* construct, *ylan* was amplified from *B. subtilis*
562 BD630 genomic DNA (*hisA1 leuA8 metB5*), using the primers 5-yfp-ylan and 3-yfp-
563 ylan. The vector pDR111-YFP was linearized by digestion with Sall and SphI. The In-
564 Fusion HD cloning kit (Clontech) was used for cloning according to manufacturer's
565 instructions. The resulting plasmid was transformed into Stellar competent cells
566 (Clontech), isolated, and verified by DNA sequence analysis performed by Eton
567 Bioscience (Union, NJ). The resulting plasmid (pED2143) was transformed into BD630
568 selecting for spectinomycin resistance, placing the *yfp-ylan* fusion under the control of
569 the isopropyl β -D-1-thiogalactopyranoside (IPTG)-inducible *P_{hyperspank}* promoter at the
570 *amyE* locus, creating the strain BD8592. The strain was confirmed by sequencing
571 performed by Eton Biosciences.

572 573 **Isolating and mapping suppressor mutations.**

574 Ten independent overnight cultures of the Δ *ylan*::*tetM* strain were cultured
575 overnight in TSB. Cultures were individually diluted 1:100 into phosphate buffered saline
576 (PBS) and 100 μ L was plated onto TSA plates with 700 μ M DIP. One colony from each
577 of the ten plates was taken and further characterized. The Δ *ylan*::*tetM* mutants with
578 suppressor mutations had growth defects indicative of the strains having a null mutation
579 in *fur*. We amplified the *fur* allele from the Δ *ylan*::*tetM* strain and each suppressor strain
580 using the 1448 veri 5 and 1448 veri 3 primer pair. After gel purification, we sequenced
581 the amplicons.

582 583 **Aconitase enzyme assay**

584 The aconitase assays were performed as previously described (50) with slight
585 modifications. *S. aureus* strains were grown in 1 mL of TSB with 0 or 120 μ M DIP for
586 four hours with shaking at 200 RPM. Cells were washed twice with PBS. A cell pellet
587 was collected by centrifugation and then stored at -80 °C before thawing and assaying.
588 Protein concentrations were determined using bicinchoninic acid (BCA) assay modified
589 for a 96-well plate (51).

590 591 **RNA-seq analysis**

592 *S. aureus* strains were cultured overnight in biological triplicates. Cultures were
593 diluted into 2.5 mL of fresh TSB to an OD_{600} of 0.05 in 10 mL culture tubes with or
594 without 120 μ M DIP and subsequently cultured for eight hours aerobically with shaking.
595 After eight hours, cultures were placed on ice, one mL of cells was harvested by

596 centrifugation, washed with PBS, resuspended in 500 μ L with RNA protect (QIAGEN),
597 pelleted by centrifugation, and stored at -80°C. RNA extraction was performed as
598 previously described (44). Cell pellets were thawed and washed twice with 0.5 mL of
599 lysis buffer (20 mM RNase-free Sodium acetate, 1 mM EDTA, 0.5% SDS). The cells
600 were lysed by the addition of 4 μ g lysostaphin and incubated for 40 min at 37°C until
601 confluent lysis was observed. RNA was isolated using TRIzol reagent according to the
602 manufacturer's instructions. RNA-seq libraries and DNA sequencing was conducted by
603 SeqCenter (Pittsburg, PA).

604 RNA-seq data were submitted to GEO and the accession identifier GSE228225
605 was provided. RNA-seq data analysis was performed using CLC Genomics Workbench
606 (Qiagen) as described previously (52). Raw data was imported and any remaining rRNA
607 reads were filtered out using the "map reads to reference" function. RNAseq analysis
608 was performed using the *S. aureus* USA300 FPR3757 genome updated to include
609 annotations for sRNAs (53). Individual differential expression analyses were performed
610 between biological triplicates and data normalized using quantile normalization. To
611 eliminate lowly expressed genes, we excluded from further analysis genes in which the
612 average expression values in both samples was less than 10 RPKM. To eliminate
613 genes with ambiguously assigned reads we excluded from further analysis genes in
614 which the percentage of assigned reads in any of the samples were less than 80%
615 unique. Genes were considered significantly altered between two strains if they
616 demonstrated a fold change >2 or <2 and a p-value <0.05 as determined by Students t-
617 test. Transcripts exhibiting significant differences in expression were placed into
618 functional categories based on their annotations in the COG database (54) as described
619 previously (55). PCA plots were generated in CLC Genomics Workbench and exported
620 to GraphPad Prism for visualization.

621 **RNA extraction, cDNA synthesis, and qPCR**

622 *S. aureus* strains were cultured overnight in TSB and subsequently diluted in
623 triplicate to an OD₆₀₀ of 0.1 in 2.5 mL TSB with or without 500 μ M DIP in 10 mL glass
624 culture tubes. Cells were incubated at 37 °C with agitation for six hours after which time
625 1 mL cell pellets were treated with RNAProtect (Qiagen). Cell pellets were washed in
626 0.5 mL PBS pH 7.4, resuspended in 100 μ L 50 mM tris pH 8 containing 6.7 μ g
627 lysostaphin, and then incubated at 37 °C with agitation for 30 minutes. The cell
628 suspension was incubated at 65 °C for 5 minutes following the addition of 200 μ L of 20
629 mM sodium acetate, 1 mM EDTA, 0.5% SDS with 13.4 μ g lysostaphin. RNA isolation
630 was performed as previously described (19). cDNA libraries were constructed using the
631 High-Capacity cDNA Reverse Transcription kit (Biosystems). Quantitative real-time
632 PCR was performed using an Applied Biosystems StepOnePlus thermal cycler. Data
633 were analyzed using the comparative C_T method (44, 56).

634 **Metabolic modeling analyses**

635 Model simulations were performed using the iYS854 genome-scale metabolic
636 model of *S. aureus* (25) as previously described (57). RNA sequencing data were
637 applied as modeling constraints using the iMAT algorithm (58, 59) using Gurobi and
638 oxygen consumption rates were applied as additional modeling constraints for sampling
639 in the COBRApy toolbox (60). The Fur deletion strain was modeled by setting the upper
640

642 bounds for Fe(II) and Fe(III) to 0 to represent model uptake derepression. DIP treatment
643 was modeling by creating sink reactions for Fe(II) and Fe(III) to represent Fe chelation.
644 Simulations were performed by sampling each model 10,000 using optGpSampler (61).
645

646 **Metabolomic analyses**

647 Strains were cultured overnight as biological triplicates before diluting into 2.5 mL
648 of fresh TSB with or without 120 μ M DIP to an OD_{600} of 0.05 in 10 mL culture tubes.
649 Cells were subsequently cultured for eight hours aerobically with shaking or statically in
650 an anaerobic chamber. After eight hours, OD_{600} was measured, and cultures were
651 placed on ice. Samples for the metabolite profiling were prepared as described
652 previously (62). Briefly, 1.5 mL of samples were collected, individual strains were
653 normalized to the lowest OD_{600} of the triplicates, cells were pelleted, and washed twice
654 with PBS. Cell pellets were resuspended in 1 mL of Methanol:Acetonitrile:Water (2:2:1)
655 solution. Cells were lysed by bead beating (2 cycles, 40 s each, 6.0 $m\ s^{-1}$) using a
656 FastPrep homogenizer (MP Biomedicals) and 0.1-mm silica glass beads (MP
657 Biomedicals). Samples were centrifuged twice at 14,500 rpm at 4 °C for 2 minutes and
658 supernatant was retained. The supernatant was filtered with nylon membrane syringe
659 filters (13 mm, 0.22 μ m, Fisherbrand) and then samples were stored at -80 °C until
660 metabolite analysis was performed.

661 Samples were analyzed at the metabolomics core of the Cancer Institute of New
662 Jersey. HILIC separation was performed on a Vanquish Horizon UHPLC system
663 (Thermo Fisher Scientific, Waltham, MA) with an XBridge BEH Amide column (150 mm
664 \times 2.1 mm, 2.5 μ m particle size, Waters, Milford, MA) using a gradient of solvent A
665 (95%:5% H_2O :acetonitrile with 20 mM acetic acid, 40 mM ammonium hydroxide, pH 9.4)
666 and solvent B (20%:80% H_2O :acetonitrile with 20 mM acetic acid, 40 mM ammonium
667 hydroxide, pH 9.4). The gradient was 0 min, 100% B; 3 min, 100% B; 3.2 min, 90% B;
668 6.2 min, 90% B; 6.5 min, 80% B; 10.5 min, 80% B; 10.7 min, 70% B; 13.5 min, 70% B;
669 13.7 min, 45% B; 16 min, 45% B; 16.5 min, 100% B; and 22 min, 100% B. The flow rate
670 was 300 μ L min^{-1} . The column temperature was set to 25 °C. The autosampler
671 temperature was set to 4 °C, and the injection volume was 5 μ L. MS scans were
672 obtained in negative mode with a resolution of 70,000 at m/z 200, in addition to an
673 automatic gain control target of 3 \times 106 and m/z scan range of 72 to 1000. Metabolite
674 data was obtained using the MAVEN software package (63) (mass accuracy window: 5
675 ppm).
676

677 **CAS siderophore assay**

678 Overnight cultures in TSB were diluted 100-fold into 1 mL of Chelex (Bio-Rad)-
679 treated TSB with the addition of 25 μ M zinc acetate, 25 μ M $MnCl_2$, 1 mM $MgCl_2$ and 100
680 μ M $CaCl_2$ in 10 mL glass culture tubes. The cultures were incubated at 37 °C with
681 shaking for 18 hours. The chrome azurol S siderophore assay was performed on the
682 spent media using the modified microplate method as previously reported (64, 65).
683

684 **Whole cell metal quantification**

685 *S. aureus* strains were grown for 18 hours overnight in TSB before diluting them to
686 an OD of 0.05 (A_{600}) in 7.5 mL of Chelex (Bio-Rad)-treated TSB in a 30 mL capacity
687 culture tubes as described previously (44). Cells were allowed to grow with shaking for

688 eight hours. Pre-weighted metal-free 15 mL propylene tubes were used to pellet the
689 cells using a prechilled tabletop centrifuge (Eppendorf, Hauppauge, NY). Pellets were
690 washed three times with 10 mL of ice-cold PBS. All samples were kept at -80 °C or on
691 dry ice until processing.

692 Cell pellets were acid digested with 2 mL of Optima grade nitric acid
693 (ThermoFisher, Waltham, MA) and 500 μ L hydrogen peroxide (Sigma, St. Louis, MO)
694 for 24 hr at 60°C. After digestion, 10 mL of UltraPure water (Invitrogen, Carlsbad, CA)
695 was added to each sample. Elemental quantification on acid-digested liquid samples
696 was performed using an Agilent 7700 inductively coupled plasma mass spectrometer
697 (Agilent, Santa Clara, CA). The following settings were fixed for the analysis Cell
698 Entrance = -40 V, Cell Exit = -60 V, Plate Bias = -60 V, OctP Bias = -18 V, and
699 collision cell Helium Flow = 4.5 mL min⁻¹. Optimal voltages for Extract 2, Omega Bias,
700 Omega Lens, OctP RF, and Deflect were determined empirically before each sample
701 set was analyzed. Element calibration curves were generated using ARISTAR ICP
702 Standard Mix (VWR). Samples were introduced by a peristaltic pump with 0.5 mm
703 internal diameter tubing through a MicroMist borosilicate glass nebulizer (Agilent).
704 Samples were initially taken at 0.5 rps for 30 s followed by 30 s at 0.1 rps to stabilize
705 the signal. Samples were analyzed in Spectrum mode at 0.1 rps collecting three points
706 across each peak and performing three replicates of 100 sweeps for each element
707 analyzed. Sampling probe and tubing were rinsed for 20 s at 0.5 rps with 2% nitric acid
708 between each sample. Data were acquired and analyzed using the Agilent Mass Hunter
709 Workstation Software version A.01.02.

710
711 **Dioxygen consumption assay.**

712 *S. aureus* strains were grown overnight in 5 mL TSB in 30 mL culture tubes at 37
713 °C in a shaker (200 RPM). Strains were diluted 1:100 into 10 mL TSB containing 0, 250,
714 500 or 750 μ M DIP in 125 mL flasks and incubated at 37 °C with agitation for four hours.
715 The cultures were diluted to an OD₆₀₀ of 0.025 in TSB containing 0, 250, 500 or 750 μ M
716 DIP prior to transfer of 200 μ L to the wells of a Seahorse XF96 V3 PS cell culture
717 microplate (Agilent). The seahorse XF sensor cartridge (Agilent) was hydrated in a non-
718 CO₂ incubator with sterile water overnight and equilibrated in XF calibrant (Agilent) for
719 two hours prior to measurement. Measurements were taken for 15 cycles with a 3-
720 minute mix and 3-minute measure cycle.

721
722 **Proton motive force measurement**

723 Overnight cultures were grown in 2 mL TSB in 10 mL culture tubes at 37 °C with
724 shaking. Strains were diluted 1:100 into 2 mL TSB +/- 500 μ M DIP and incubated at 37
725 °C with shaking for six hours. Cell pellets were collected from 2 mL of culture and
726 washed with 0.5 mL PBS, pH 7.4, and then resuspended in 0.5 mL PBS. The OD₆₀₀
727 was adjusted to 0.085 in PBS. Thirty micromolar 3,3'-diethyloxacarbocyanine iodide
728 (DiOC₂(3)) +/- 5 μ M carbonyl cyanide m-chlorophenyl hydrazone (CCCP) were added to
729 the cell suspension followed by incubation at room temperature for 30 minutes.
730 Fluorescence (excitation of 450 nm, emission of 670 nm) was measured using a
731 Varioskan Lux plate reader (Thermo Scientific).

732
733 **Transcriptional reporter assays.**

734 Overnight cultures of *S. aureus* strains were grown overnight in 2 mL TSB
735 supplemented with 10 μ g mL⁻¹ chloramphenicol in 10 mL culture tubes at 37 °C with
736 shaking. *S. aureus* cultures were then subcultured 1:100 into 5 mL TSB supplemented
737 with 10 μ g mL⁻¹ chloramphenicol +/- 500 μ M DIP in 10 mL culture tubes and incubated
738 at 37 °C with shaking for 8 hours. OD₆₀₀ and GFP fluorescence (excitation 485 nm,
739 emission 520 nm) were measured using a Varioskan Lux plate reader (Thermo
740 Scientific). GFP fluorescence relative to OD₆₀₀ was determined. The assay was
741 performed in triplicate.

742

743 Bioinformatic analyses

744 The predicted protein sequences from all assembled bacterial genomes
745 designated as "reference" or "representative" in the NCBI database were retrieved on
746 03/14/2023. The *Staphylococcus aureus* YlaN sequence (ABD22267.1) was used as a
747 query for a DIAMOND (v2.1.2; '--ultra-sensitive --max-target-seqs 0') (66) search
748 against the bacterial proteins retrieved from NCBI. Only hits with an e-value < 1e⁻⁵ were
749 retained for downstream analysis; bacterial genomes that encode proteins with hits (e-
750 value < 1e⁻⁵) to the YlaN query were considered YlaN-positive. Four Fur sequences
751 (ABD21033.1, P54574, P0C6C8, P0A9A9), two from the species of interest in this study
752 and two from species known to not encode YlaN, were used as queries for a DIAMOND
753 (v2.1.2; '--ultra-sensitive --max-target-seqs 0') search against the bacterial proteins
754 retrieved from NCBI. Only hits with an e-value < 1e⁻⁵ were retained for downstream
755 analysis. The hits from each of the four Fur query sequences were parsed separately,
756 retaining the best (highest scoring) hit per genera. The top-scoring sequences (one per
757 genera in the output) from each of the queries were combined and had redundant
758 sequences (those identified by multiple queries) removed. The combined non-redundant
759 sequences were aligned using mafft (v7.453; '--localpair --maxiterate 1000') (67), with
760 the resulting alignment used by fastme (v2.1.5) (68) for phylogenetic inference. Gotree
761 (v0.4.4) and Goalign (v0.3.6) (69) were used for file format conversion between analysis
762 steps and iTOL (70) was used for visualization. The filtering approach (down sampling
763 to genera) applied to the Fur hits was performed to reduce the number of sequences to
764 an amount that is computational tractable for phylogenetic analysis (i.e., it reduced the
765 number of sequences in the resulting phylogeny from 10's of thousands to only a few
766 thousand).

767 The sequences that form the large clade of Firmicutes Fur sequences (Figure 7)
768 were extracted for reanalysis. The protein sequences were realigned using mafft ('--
769 localpair --maxiterate 1000') and had a phylogeny inferred using iqtree (v1.6.12; '-m
770 MFP -bb 2000'). The alignment and phylogeny were compared together visually using
771 iTOL. To improve readability a phylogeny with a reduced number of taxa (10% chosen
772 at random from the full phylogeny) was also constructed and visualized using the same
773 approach (Figure S11). A phylogeny of the Fur sequences from genomes which encode
774 YlaN sequences (YlaN-positive genomes), and a phylogeny of the YlaN sequences
775 from these genomes, were inferred from the Firmicutes extracted from Figure 7, with
776 mafft and iqtree used for alignment and phylogeny inference (using the same versions
777 and parameters as previously stated). Fur and YlaN sequences from genomes with
778 multiple Fur or YlaN genes identified (using the previously described DIAMOND search
779 results) were removed to prevent problems arising from paralogous sequences. The Fur

780 and YlaN trees were compared using the tanglegram function ('sort=TRUE,
781 rank_branches=TRUE') from the dendextend (v1.17.1) R package (71).

782 To map changes in gene expression to the KEGG pathway maps, the predicted
783 proteins for *Staphylococcus aureus* subsp. USA300_FPR3757 were downloaded from
784 NCBI (NC_007793) and assigned KEGG Orthology (KO) numbers using the KEGG
785 Automatic Annotation Server (gene dataset: *Staphylococcus aureus* USA300_FPR3757
786 [saa], search tool: BLAST) (72). The NCBI gene IDs were manually assigned to the old
787 *Staphylococcus aureus* gene names used for expression analysis and used to transfer
788 KO number annotations.

789 The structural model of *Staphylococcus aureus* Fur-YlaN complexes were built
790 with ColabFold v.1.5.2: AlphaFold2 (Deep Mind) using MMseq2 (Max-Planck Institute
791 for Biophysical Chemistry) (73) using the following amino acid sequences: ABD21033.1
792 and ABD22267.1. Five models were generated with three recycles. The final models
793 were energy-minimized with Amber.

794

795 **YlaN interaction experiments**

796 *Immunopurification of YFP-YlaN.* *B. subtilis* strain BD8592 was grown overnight
797 in 50 mL of LB with 100 μ g mL⁻¹ spectinomycin. After incubation, cells were diluted
798 1:100 (v/v) into 2 L of fresh LB media with the addition of 0.5 mM isopropyl- β -d-1-
799 thiogalactosidase (IPTG) and grown for 1.5 hours for exponential phase or 4 hours for
800 stationary phase. Growth was monitored hourly by the optical density at OD₆₀₀. Cells
801 were harvested by centrifugation, frozen as pellets in liquid nitrogen, and subjected to
802 cryogenic cell lysis as described previously (27). 0.75 g of frozen cell powder was
803 immediately added to 10 mL of lysis buffer (20 mM HEPES, pH 7.4, 100 mM potassium
804 acetate, 2 mM MgCl₂, 0.1% tween-20 (v/v), 1 μ M ZnCl₂, 1 μ M CaCl₂, 0.25% Triton-X,
805 200 mM NaCl, 1:100 protease inhibitor cocktail (Sigma) and 0.1 mg mL⁻¹
806 phenylmethylsulphonyl fluoride (PMSF)). The resulting suspension was homogenized
807 for 20 s using a PT 10-35 GT Polytron (Kinematica) and centrifuged for 10 min at 8000
808 x g at 4°C. The soluble fraction was mixed with 10 μ L of GFP-Trap magnetic agarose
809 (Proteintech) for 1 h with gentle rotation at 4°C. The magnetic beads were recovered
810 and washed four times with lysis buffer without inhibitors and two times with PBS.
811 Proteins were eluted directly into 50 μ L of TEL buffer (106 mM Tris-HCl, 141 mM Tris-
812 base, 0.5 mM EDTA, 2.0% LDS, pH 8.5) for in-solution digestion (74, 75).

813 *Preparation of samples for mass spectrometry.* Samples were alkylated and
814 reduced with final concentrations of 30 mM chloroacetamide and 10 mM Tris(2-
815 carboxyethyl)phosphine hydrochloride (TCEP, pH 7.0), and heated to 95 °C for 5
816 minutes. Protein digestion was performed using a filter-aided sample preparation
817 method (FASP), (76-78). Briefly, filters [Vivacon 500 centrifugal filters (10K cut-off),
818 Sartorius Stedim Biotech, Goettingen, Germany] were used for desalting and overnight
819 trypsin digestion at 37°C with a 1:50 enzyme to protein ratio in 40 mM HEPES, pH 7.4,
820 0.1% sodium deoxycholate. Following digestion, the detergent was removed from the
821 samples through acidification with 1% trifluoroacetic acid (TFA, final concentration) as
822 described (79, 80). Soluble peptides were desalted using SDB-RPS Stage Tips and
823 eluted in 50 mL of 5% ammonium hydroxide-80% acetonitrile (ACN) (81). Samples were
824 evaporated to near dryness by vacuum centrifugation and resuspended in 1% formic
825 acid (FA)/4% ACN to bring the total volume to 10 mL.

826 *Mass spectrometry.* Samples were analyzed by nano-liquid chromatography-
827 tandem mass spectrometry (nLC-MS/MS) on a Dionex Ultimate 3000 RSLC coupled
828 directly to an LTQ-Orbitrap Velos mass spectrometer (ThermoFisher Scientific, San
829 Jose, CA), through a Nanospray Flex ion source (ThermoFisher Scientific).
830 Approximately 4 μ L of peptides were directly injected for analysis. Instrument
831 parameters and settings were as described previously (82), except peptides were
832 separated using a 150 min linear reverse phase gradient. The mass spectrometer was
833 operated in a data-dependent acquisition mode with each cycle of analysis containing a
834 single full-scan mass spectrum (m/z = 350–1700) in the orbitrap (r = 120,000 at m/z =
835 400) followed by collision-induced dissociation (CID) MS/MS of the top 15 most
836 abundant ions, with dynamic exclusion enabled.

837 *Informatics workflow.* The MS/MS spectra were extracted using the Proteome
838 Discoverer software platform (ver. 1.4, ThermoFisher Scientific). All spectra were
839 subsequently analyzed using SEQUEST (ver. 1.4.0.288, ThermoFisher Scientific) and
840 X! Tandem (ver. CYCLONE (2010.12.01.1), The GPM, thegpm.org) for database
841 searching against the UniProt SwissProt sequence database (downloaded 04/2017)
842 comprised of *Bacillus subtilis* and *Escherichia coli* reference proteome sequences,
843 including common contaminant sequences (total of 8604 sequences). X! Tandem was
844 set up to search a reverse concatenated subset of the same database. The processing
845 workflow parameters were defined as follows: peptides with at least 6 amino acids, full
846 trypsin cleavage specificity, and up to 2 missed cleavages. Database searching was
847 performed with precursor and fragment ion mass tolerances of 10 parts per million
848 (ppm) and 0.4 Da, respectively. Cysteine carbamidomethylation was denoted as a fixed
849 modification and methionine oxidation, asparagine deamidation, phosphorylation of
850 serine and threonine, lysine acetylation, and n-terminal acetylation, as variable
851 modifications. Peptide and protein identifications were validated using Scaffold (ver.
852 4.8.1, Proteome Software, Inc.), with a peptide and protein false discovery rate (FDR)
853 threshold of < 1.0%. For label-free quantification, the intensity based on the sum of the
854 three highest intensity peptides for each protein (T3PQ) was used (83).

855

856 **YlaN purification**

857 *E. coli* strain BL21(DE3) containing pGEX-6P-1_ylaN was cultured in 3 L of 2X
858 LB supplemented with ampicillin (50 μ g mL⁻¹) at 30°C with shaking. After reaching an
859 OD₆₀₀ of 0.5, the temperature was shifted to ~25°C and ylaN expression was induced
860 with 100 μ M IPTG for ~16 hrs. The cells were harvested by centrifugation and
861 resuspended in purification buffer (150 mM NaCl, 50 mM Tris-HCl, pH 7.5) containing
862 1% weight per volume lysozyme. Cells were disrupted using a French pressure cell and
863 cell debris removed by centrifugation. The cell free extract was filtered through a 0.45
864 μ M filter before loading into a 5 mL glutathione Sepharose 4 fast flow column (Cytiva).

865 The GST column was equilibrated with purification buffer and filtered extract was
866 loaded onto the column. The column was washed with 25 column volumes of
867 purification buffer. After washing, the column was incubated with 1 column volume of
868 cleavage buffer (50 mM Tris-HCl, pH 7.0, 150 mM NaCl, 1 mM EDTA, 1 mM
869 dithiothreitol containing PreScission Protease (Cytiva). Following overnight incubation,
870 YlaN was eluted using 5 mL of cleavage buffer. Eluted protein was concentrated using
871 spin concentrators (Millipore Amicon Ultra-15 -3K) to ~1.5-2 mL and subsequently

872 dialyzed in one liter of storage buffer (150 mM NaCl, 50 mM Tris-HCl, pH 7.5, 5% (v/v)
873 glycerol) three individual times to remove EDTA. YlaN was flash frozen and stored at
874 -80°C until use. Protein concentration was measured using a BCA assay.
875

876 **Fe-Binding Competition Assay**

877 The ferrous ion binding affinity of YlaN was measured as previously reported
878 (29). Briefly, this assay exploits Mag-Fura-2 (Molecular Probes) as a metal chelator
879 chromophore to measure the binding of ferrous ions to an additional biomolecule (i.e.,
880 YlaN) under complex heterogeneous conditions. Mag-Fura-2 forms a 1:1 complex with
881 Fe(II) and displays a maximum absorbance at 325 nm when metal is bound; this is in
882 contrast to a feature at 365 nm when the chelator is in the apo state (29, 30, 32). The
883 transition of the absorbance feature at 365 nm, observed during metal loading of YlaN,
884 was measured using a Shimadzu UV-1800 spectrophotometer housed within a Coy
885 anaerobic chamber. Titration data for adding a divalent metal ion into the protein/Mag-
886 Fura-2 mixture were collected anaerobically at room temperature using a 1 cm quartz
887 cuvette. All spectra were collected anaerobically in 20 mM Tris, 150 mM NaCl (pH 7.5)
888 buffer.

889 Samples were prepared for analysis in the following manner. Reagents/buffers
890 were Ar(g) purged and equilibrated overnight within a Coy anaerobic wet chamber prior
891 to experimentation. Holo- and apo-protein solution samples were prepared immediately
892 before use under the same buffer and maintained under anaerobic conditions.
893 Independent protein samples, incubated in 5 mM TCEP prior to titrations, were dialyzed
894 using anaerobic buffer before analysis to remove the TCEP. Mag-Fura-2 concentrations
895 were varied between 1 and 4 μ M, while the protein concentration was held constant at 2
896 μ M. A solution of 2 mM ammonium ferrous sulfate hexahydrate, prepared in the
897 anaerobic buffer listed previously was added in progressive increments until absorption
898 saturation was reached. After each addition of aqueous ferrous ions, an absorption
899 spectrum was collected between the wavelength of 200-800 nm. Initial apo Mag-Fura-2
900 concentrations were determined using the molar absorptivity (ϵ) value of 29,900 $M^{-1}cm^{-1}$
901 for the compound, measured at the wavelength of 365 nm (28). The absorbance at 365
902 nm, corrected for dilution, was then used to calculate binding parameters. Binding data
903 were simulated with the program DYNAFIT (84), using a non-linear least squares
904 analysis script to identify the binding capacity and metal stoichiometry in a manner
905 previously outlined (28, 30). Each titration experiment was simulated using both one
906 and two-site metal binding models.
907

908 **Circular Dichroism Spectroscopy**

909 Apo- and holo-YlaN samples were characterized for secondary structure content
910 using a Jasco 1500 spectrophotometer as described previously (30). Briefly, samples
911 were prepared anaerobically in a Coy wet chamber, loaded into a 0.1 cm quartz cuvette,
912 then transferred to the nitrogen purged sample chamber of the instrument where data
913 was collected at 27 °C. Spectra were collected on 5 - 10 μ M protein concentration
914 samples 5 mM NaPO₄ buffer solutions at pH 7.5. For reproducibility, an average of thirty
915 scans were collected on three samples per state and results were averaged for final
916 analysis. Before spectral collection, a baseline at each wavelength was subtracted to
917 eliminate buffer signal. Data were analyzed using the Jasco CD Pro analysis software

918 and simulated using the CONTIN method including the SP29, SP37, SP43, SMP50 and
919 SMP56 reference sets (31). Values obtained from simulations using each database
920 were averaged to obtain final analysis parameters.

921

922 **Differential Scanning Calorimetry**

923 Thermal stability parameters for apo- and holo-YlaN were evaluated using a VP
924 Differential Scanning Calorimeter (TA Instruments) housed anaerobically in a Coy wet
925 chamber. Protein and iron solutions were prepared anaerobically in 20 mM Tris, 150
926 mM NaCl solution at a pH of 7.5. Buffer was independently degassed with argon prior to
927 sample preparation and loading. Protein concentrations between 3-5 mg mL⁻¹ were
928 used, and a 2.0 mM ferrous ion solution was added to obtain samples up to a 1:1
929 protein to Fe ratio at a final volume of 600 μ L. DSC scans were run at a rate of 1 °C per
930 minute over a temperature range of 10-90 °C. Pressure was maintained above 2.95 atm
931 throughout the scan. Data were analyzed using the Nano Analyze software provided by
932 TA Instruments. Baseline subtraction of buffer alone or buffer with iron at concentrations
933 that matched the protein samples were measured as controls. Peak deconvolution of
934 the protein spectra was achieved using the two-state scaled mathematical model that
935 incorporates the A_w factor, which accounts for inaccuracies in protein concentration
936 upon denaturation. Data presented represents an average of three sample results.

937

938 **X-Ray Absorption Spectroscopy**

939 Fe(II)-YlaN samples were prepared in 20 mM Tris and 150 mM NaCl. The
940 sample was brought to a 30% glycerol concentration for cryo-protection, and samples
941 were flash frozen and stored in liquid nitrogen immediately after loading into
942 prewrapped 2 mm Leucite XAS cells until exposed to the beam. Fe XAS was collected
943 at the Stanford Synchrotron Radiation Lightsource (SSRL) on beamline 7-3. This
944 beamline is equipped with a Si[220] double crystal monochromator with a mirror present
945 upstream for focusing and harmonic rejection. We used a Canberra 30 element
946 germanium solid state detector to measure protein fluorescence excitation spectra.
947 Temperature during collection was maintained at 10 K by an Oxford Instruments
948 continuous-flow liquid helium cryostat and data was collected with the solar slits utilizing
949 a 3 μ m Mn filter placed between the cryostat and detector to diminish background
950 scattering. XAS spectra were collected in 5 eV increments in the pre-edge region, 0.25
951 eV increments in the edge region, and 0.05 Å⁻¹ increments in the EXAFS region to $k =$
952 14 Å⁻¹, integrated from 1 to 25 s in a k^3 -weighted manner for a total scan length of ~40
953 min. Fe foil absorption spectra were simultaneously collected with each respective
954 protein run, and used for calibration and assigning first inflection points for the metals
955 (7,111.2eV)

956

957 XAS spectra were processed and analyzed using the EXAFSPAK program suite
958 written for Macintosh OS-X (85), integrated with the Feff v8 software (86) for theoretical
959 model generation. Normalized XANES data was subjected to edge analysis for both
960 metals and in the case of Fe, to pre-edge analysis as well. The Fe 1s-3d pre-edge peak
961 analysis was completed as described previously (87); peak area was determined over
962 the energy range of 7,110–7,116 eV. Oxidation state was deduced from the first
963 inflection energies of the respective edges (32). Data were collected to $k = 14$ Å⁻¹, which
964 corresponds to a spectral resolution of 0.121 Å⁻¹ for all metal-ligand interactions (32);

964 therefore, only independent scattering environments at distances $>0.121\text{ \AA}$ were
965 considered resolvable in the EXAFS fitting analysis. Data were fit using both single and
966 multiple scattering model amplitudes and phase functions to simulate Fe-O/N, -S, and -
967 Fe ligand interactions. During Fe data simulations, a scale factor (Sc) of 0.95 and
968 threshold shift (ΔE_0) value of -10 eV (Fe–O/N/C), -12 eV (Fe–S) and -15 eV (Fe–Fe)
969 were used. These values were obtained from fitting crystallographically characterized
970 small molecule Fe (87). The best-fit EXAFS simulations were based on the lowest mean
971 square deviation between data and fit, corrected for the number of degrees of freedom
972 (F') (88). During the standard criteria simulations, only the bond length and Debye-
973 Waller factor were allowed to vary for each ligand environment.
974

975 **Figure legends**

976
977 **Figure 1. A role for YlaN in Fe ion homeostasis. Panel A:** Growth of the WT
978 (JMB1100) and Δ *ylaN::tetM* (JMB8689) with pCM28 or pCM28_ylaN on TSA-Cm with or
979 without 2,2-dipyridyl (DIP) or EDDHA. Overnight cultures were grown in TSB, serial
980 diluted, and spot plated. Plates were incubated for 18 hours before visualization.
981 Pictures of a representative experiment are displayed. **Panel B:** Growth of the WT and
982 Δ *ylaN::tetM* strains in Chelex-treated TSB medium supplemented with trace metals
983 lacking Fe with and without 40 μ M Fe(II). Data represent the average of biological
984 triplicates and errors are displayed as standard deviations. **Panel C:** Streptonigrin
985 sensitivity was monitored using TSB-Cm top-agar overlays enclosing the WT or
986 Δ *ylaN::tetM* strains containing either pEPSA5 or pEPSA5_ylaN. The data in panels B
987 and C represent the average of three biological replicates with standard deviations
988 displayed. Student's t-tests were performed on the data in panel C and * indicates $p <$
989 0.05.

990
991 **Figure 2. Null fur mutation bypasses the essentiality of YlaN in Fe-deplete**
992 **conditions. Panel A:** Overnight cultures of the WT (JMB1100), Δ *ylaN::tetM* (JMB8689),
993 Δ *ylaN::tetM fur** (JMB10678), *ylaN::Tn fur::tetM* (JMB10641), and *ylaN::Tn* (JMB8428)
994 strains were serial diluted and spot plated on TSB media with or without 2,2-dipyridyl
995 (DIP) or EDDHA. **Panel B:** Overnight cultures of the WT, Δ *ylaN::tetM*, Δ *ylaN::tetM fur**,
996 and *ylaN::Tn fur::tetM* strains containing either pOS or pOS_fur were serial diluted and
997 spot plated on TSB-Cm media with or without DIP. **Panel C:** The 57 Fe load was
998 quantified in whole cells using ICPMS after culture in TSB medium. The ratio of 57 Fe /
999 78 Se is displayed for the *proC::Tn* (JMB10675), Δ *ylaN::tetM proC::Tn* (JMB10677), *fur**
1000 *proC::Tn* (JMB10676), and Δ *ylaN::tetM fur* proC::Tn* (JMB10678) strains. **Panel D:**
1001 Streptonigrin sensitivity was monitored using top-agar tryptic soy agar overlays
1002 enclosing the *proC::Tn*, Δ *ylaN::tetM proC::Tn*, and *fur* proC::Tn*, and Δ *ylaN::tetM fur**
1003 *proC::Tn* strains. Five μ L of 2.5 mg mL⁻¹ streptonigrin was spotted upon the overlays
1004 and the area of growth inhibition was measured after 18 hours of growth. Pictures of
1005 representative experiments are displayed in Panels A and B after 18 hours of growth.
1006 The data in panels C and D represent the average of three biological replicates with
1007 standard deviations displayed. Student's t-tests were performed on the data in panels C
1008 and D. * indicates $p < 0.05$.

1009
1010 **Figure 3. Transcriptome analyses suggest Fur-dependent transcriptional changes**
1011 **redirecting central metabolism upon Fe limitation. Panel A:** Volcano plots of genes
1012 that have a Log2 fold change of ≥ 2 or ≤ -2 in the Δ *fur::tetM* (JMB1432) strain compared
1013 to the WT (JMB1100). **Panel B:** Volcano plots of genes that have a Log2 fold change of
1014 ≥ 2 or ≤ -2 in the 2,2-120 μ M dipyridyl (DIP) challenged WT strain compared to
1015 unchallenged. **Panel C:** Dioxygen consumption rates (OCR) of the WT (JMB1100) and
1016 Δ *fur::tetM* (JMB1432) strains cultured in TSB media with and without 2,2-dipyridyl (DIP).
1017 OCR was monitored using a Seahorse Analyzer. **Panel D:** The membrane potentials of
1018 the WT and Δ *fur::tetM* strains were measured using the fluorescent dye 3'3'-
1019 diethyloxacarbocyanine iodide (DiOC₂) after culture in TSB media with and without 2,2-
1020 dipyridyl (DIP). The data presented represent the average of biological triplicates.

1021 Standard deviations are displayed in Panels C and D and Student's t-tests were
1022 performed and * indicates $p < 0.05$.
1023

1024 **Figure 4. Genome-scale metabolic modeling analyses suggest Fe limitation**
1025 **induces fermentation. Panels A and B:** Modeling analyses predict decreased
1026 respiratory activity (Panel A) and TCA cycle activity (Panel B). Flux balance analysis
1027 was performed on the iYS854 genome-scale metabolic model of *S. aureus* using
1028 transcriptome and dioxygen consumption measurements for WT, DIP-treated cells, and
1029 $\Delta fur::tetM$ strains as modeling constraints. **Panel C:** AcnA activity in cell-free lysates
1030 generated from the WT and $\Delta fur::tetM$ strains after four hours of culture with (green
1031 bars) and without (blue bars) 120 μ M DIP. **Panel D:** Modeling analyses predict
1032 increased activity in acetate fermentation. For modeling analyses, data represent
1033 distributions for metabolic reaction activity simulations using 10,000 sampling points.
1034 Black lines represent median values for each distribution. For aconitase experiments,
1035 data represent the average of three biological replicates with standard deviations
1036 displayed. Kruskal-Wallis tests were performed on data in panels A, B, and C. Student's
1037 t-tests were performed on the data in panel C. * indicates $p < 0.05$ and **** indicates $p <$
1038 0.0001.
1039

1040 **Figure 5. Fermentative growth bypasses the need for YlaN in Fe-deplete**
1041 **conditions. Panels A and B:** The *proC::Tn* (JMB10675), $\Delta ylaN::tetM$ *proC::Tn*
1042 (JMB10677), *fur* proC::Tn* (JMB10676), and $\Delta ylaN::tetM$ *fur* proC::Tn* (JMB10678)
1043 strains were cultured overnight before serial dilution and spot plating on TSA with and
1044 without 2,2-dipyridyl (DIP). The cultures displayed in panel A were incubated aerobically
1045 and the cultures in panel B were incubated anaerobically in the absence of a terminal
1046 electron acceptor to force fermentative growth. Photographs of a representative
1047 experiment are shown. **Panels C and D:** The WT (JMB1100) and $\Delta fur::tetM$ (JMB1432)
1048 strains were inoculated into TSB medium with and without DIP or EDDHA before
1049 culturing overnight aerobically or anaerobically in the absence of a terminal electron
1050 acceptor. Culture optical densities were recorded after 18 hours of growth. The data
1051 displayed represent the average of biological triplicates and standard deviations are
1052 displayed. Student's t-tests were performed on the data and * indicates $p < 0.05$.
1053

1054 **Figure 6. The presence of YlaN promotes Fur-dependent derepression in Fe-**
1055 **deplete conditions. Panels A-D:** The transcriptional activities of the *isdC*, *fhuC*, *tsr25*,
1056 and *sbnA* promoters were measured in the WT (JMB1100), $\Delta ylaN::tetM$ (JMB8689), and
1057 $\Delta fur::tetM$ (JMB1432) strains after culture in TSB-Cm media with (blue bars) and without
1058 (orange bars) 500 μ M 2,2-dipyridyl (DIP). We were unable to mobilize the *sbnA*
1059 transcriptional reporter into the *fur::tetM* strain. The data displayed represent the
1060 average of biological quintets and standard deviations are displayed. **Panels E-I:**
1061 Abundances of RNAs expressed from select Fur-regulated genes in the WT and
1062 *ylaN::tetM* strains were determined using quantitative PCR after culture in TSB media
1063 with and without 500 μ M DIP. The data displayed represent the average of biological
1064 triplicates and standard deviations are displayed. **Panel J:** The ability of cell free culture
1065 spent medium to compete with chrome azurol S (CAS) for Fe was measured
1066 spectrophotometrically. Cell free spent culture medium was harvested from the *proC::Tn*

1067 (JMB10675), $\Delta ylaN::tetM$ $proC::Tn$ (JMB10677), fur^* $proC::Tn$ (JMB10676), and
1068 $\Delta ylaN::tetM$ fur^* $proC::Tn$ (JMB10678) strains after culture in Chelex-treated TSB. The
1069 data displayed represent the average of biological triplicates with standard deviations
1070 shown. Student's t-tests were performed on the data and * indicates $p < 0.05$.
1071

1072 **Figure 7. Phylogeny of representative bacterial Fur sequences.** Tree (midpoint
1073 rooted) constructed using fastme from Fur sequences, down sampled to a genera level,
1074 extracted from high-quality representative or reference bacterial genomes. For each
1075 sequence in the tree, the colors in the surrounding rings represent the (inner ring)
1076 phylum, (middle ring) presence or absence of YlaN in the genome from which the Fur
1077 sequence was derived, and (outer ring) annotated metal-binding affinity. A legend
1078 showing the colors used in the surrounding rings is shown on the left side of the image,
1079 as is the branch length scale.
1080

1081 **Figure 8. YlaN is an Fe(II) binding protein. Panel A:** Fe binding affinity to YlaN
1082 measured using Mag-Fura-2 within a competition-based assay. Average titration
1083 spectral points of Fe(II) ions into YlaN with overall simulation in solid line. Mag-fura-2 to
1084 protein ratios were varied and 1:1 data is shown. Spectra were collected in duplicate
1085 using independent samples to ensure spectral reproducibility. **Panel B:** Circular
1086 dichroism (CD) Structural results for apo and Fe(II) loaded holo-YlaN. Representative
1087 CD spectra comparing apo- (black) and holo- (blue) YlaN. **Panel C:** Differential
1088 scanning calorimetric spectra for apo- and Fe(II) loaded holo-YlaN. Overall simulation of
1089 molar heat capacity vs. temperature spectra for apo- (a) and holo- (b) YlaN. Overall
1090 simulations are displayed in solid lines, with individual simulated features in gray and
1091 raw data shown in a black dashed line.
1092

1093 **Figure 9. Examining the YlaN Fe(II) ligand environment. Panel A:** Normalized
1094 XANES for Fe(II) bound to YlaN. Representative spectra for Fe XANES for Fe-YlaN
1095 (left) and extended display of Fe-XANES pre-edge region (right). **Panel B:** EXAFS
1096 analyses of Fe(II) bound YlaN. Raw EXAFS, Fourier transforms of EXAFS, and spectral
1097 simulations for Fe(II) bound YlaN. Fe EXAFS data and simulation of YlaN. Raw k^3
1098 weighted EXAFS data (left) and phase shifted Fourier transform (FT) (right) are shown.
1099 Raw data is shown in black, and simulations in green.
1100

1101 **Figure 10. Working model for YlaN function.** In our model, Fur (purple) and YlaN
1102 (pink) bind Fe(II) transiently. They are both metalated in Fe replete growth conditions
1103 and Fur directly prevents transcription of genes coding for Fe acquisition machinery.
1104 Upon Fe limitation, YlaN forms a complex with Fur and aids Fe(II) removal.
1105 Demetallated Fur has a decreased affinity for DNA and no longer acts as a
1106 transcriptional repressor. Fur derepression causes increased expression of genes
1107 coding for Fe acquisition systems and indirectly (broken line) decreases expression of
1108 genes coding for Fe requiring enzymes and processes.
1109
1110

1111 **Supplemental Figure legends**
1112

1113 **Figure S1.** Growth of the wild type and $\Delta ylaN::tetM$ strains in TSB medium. Overnight
1114 cultures of the wild type (JMB1100) and the $ylaN::tetM$ mutant (JMB8689) were diluted
1115 1:1000 into 5 mL of fresh TSB in 25 mL capacity culture tube. Cells were cultured at 37
1116 °C with shaking at 200 rpm.

1117
1118 **Figure S2.** The ^{57}Fe load was quantified in whole cells using ICPMS after culture in
1119 TSB medium. The ratio of ^{57}Fe / ^{31}P is displayed for the $proC::Tn$ (JMB10675),
1120 $\Delta ylaN::tetM proC::Tn$ (JMB10677), and $fur^* proC::Tn$ (JMB10676), and $\Delta ylaN::tetM fur^* proC::Tn$ (JMB10678) strains. Student's t-tests were performed on the data and *
1121 indicates $p < 0.05$.
1122

1123
1124 **Figure S3.** Growth of the WT (JMB1100), $\Delta ylaN::tetM$ (JMB8689), $\Delta ylaN::tetM fur^*$
1125 (JMB10678), $fhuC::Tn$ (JMB7525), $\Delta ylaN::tetM fhuC::Tn$ (JMB10721), $\Delta ylaN::tetM fur^* fhuC::Tn$ (JMB10722) strains with or without 2,2-dipyridyl (DIP) or EDDHA. Overnight
1126 cultures were grown in TSB, serial diluted, and spot plated. Pictures of a representative
1127 experiment are displayed.
1128

1129
1130 **Figure S4.** PCA plot of significantly altered RNA abundances in the wild type (WT;
1131 JMB1100) and $\Delta fur::tetM$ (JMB1432) strains after culture in TSB media with and without
1132 150 μM 2,2-dipyridyl. RNAs were isolated from biological triplicates.
1133

1134
1135 **Figure S5.** A plot of the Log2 fold change determined by RNA sequencing was plotted
1136 against the Log2 fold change determined using qPCR.
1137

1138
1139 **Figure S6.** A Venn diagram displaying the transcriptional overlap between the WT
1140 (JMB1100) vs $\Delta fur::tetM$ (JMB1432) regulon and the WT vs WT + 150 μM 2,2-dipyridyl
(DIP) regulon.
1141

1142
1143 **Figure S7.** The abundances of select RNAs of the WT (JMB1100) and $\Delta fur::tetM$
1144 (JMB1432) after growth in TSB with and without 150 μM 2,2-dipyridyl (DIP). Normalized
1145 RNA reads were from RNA sequencing data.
1146

1147
1148 **Figure S8.** Transcripts exhibiting significant differences in expression in the WT
1149 (JMB1100) vs $\Delta fur::tetM$ (JMB1432) (Panel A) and the WT vs WT + 150 μM 2,2-
1150 dipyridyl (DIP) (Panel B) regulons were placed into functional categories based on their
1151 annotations in the COG database.
1152

1153
1154 **Figure S9.** A $hemB::Tn$ mutant is defective in respiration and generating a proton
1155 motive force. **Panel A:** Dioxygen consumption rates (OCR) of the WT (JMB1100) and
1156 $hemB::Tn$ (JMB4536) strains cultured in TSB medium. **Panel B:** The membrane
1157 potentials of the WT and $hemB::Tn$ strains were measured using the fluorescent dye
1158 3'3'-diethyloxacarbocyanine iodide (DiOC₂). Overnight cultures were grown in tryptic soy
1159 broth (TSB). Cells were washed with phosphate buffered saline (PBS) pH 7.4 and then
1160 resuspended in 0.5 mL PBS pH 7.4. Thirty micromolar 3,3'-diethyloxacarbocyanine
1161 iodide (DiOC₂(3)) +/- 5 μM carbonyl cyanide m-chlorophenyl hydrazone (CCCP) were
1162 added to the cell suspensions followed by incubation at room temperature for 30
1163

1159 minutes. Fluorescence (excitation of 450 nm, emission of 670 nm) was measure. All
1160 data represent the average of biological triplicates and standard deviations are
1161 displayed. Student's t-tests were performed on the data and * indicates $p < 0.05$.
1162

1163 **Figure S10.** The abundances of RNAs from the WT (JMB1100) and $\Delta fur::tetM$
1164 (JMB1432)

1165 strains were determined using quantitative PCR. Fold changes were determined using
1166 the $\Delta\Delta Ct$ method. Student's t-tests were performed on the data and * indicates $p < 0.05$.
1167

1168 **Figure S11:** Down sampled phylogeny and associated alignment of Firmicutes Fur
1169 sequences. Sequences were randomly chosen from those in the Firmicutes Fur clade
1170 (Figure 7) to facilitate visualization of the relationship (tree shown on left side of the
1171 figure) between the YlaN-positive (black bars in the middle of the figure) and -negative
1172 sequences and their associated aligned protein sequences (left side of the figure;
1173 residues colored using the clustal scheme). Phylogeny were constructed using
1174 maximum-likelihood with automatic model selection and node support tested via 2,000
1175 ultrafast phylogenetic bootstraps.
1176

1177 **Figure S12:** Tanglegram of Firmicutes Fur and YlaN proteins. Phylogenies of
1178 Firmicutes Fur (left) and YlaN (right) proteins from YlaN-positive genomes. Lines are
1179 used to connect the same tips in each tree, with groups of tips from clades shared
1180 between both trees shown using colored lines. Phylogenies were constructed using
1181 maximum-likelihood with automatic model selection and node support tested via 2,000
1182 ultrafast phylogenetic bootstraps. Branch lengths have been scaled and only nodes with
1183 $\geq 95\%$ bootstrap support are annotated to improve readability.
1184

1185 **Figure S13.** AlphaFold2 structural models of the Fur-YlaN complex. **Panel A:** Surface
1186 representation of the complex modeled in one-to-one stoichiometry. YlaN (ABD22267.1)
1187 is displayed in pink and Fur (ABD21033.1) in shown in purple. Some of the conserved
1188 residues of YlaN helix two are highlighted in yellow. **Panel B:** Surface representation of
1189 the Fur-YlaN complex modeled in two to one stoichiometry. **Panel C:** The predicted
1190 Local Distance Difference Test (pLDDT) values calculated for five AlphaFold2 ranked
1191 models. The “rank 1” model of the Fur-YlaN complex formed in one-to-one
1192 stoichiometry is presented in Panel A. **Panel D:** The Local Distance Difference Test
1193 (LDDT) values calculated for five AlphaFold2 ranked models. The “rank 1” model of the
1194 Fur-YlaN complex formed in two to one stoichiometry is presented in Panel B. The
1195 accuracy of all AlphaFold2 predictions is reflected by high pLDDT values, in particular
1196 those obtained for Fur.
1197

1198 **Table Legends**

1201 **Table S2.** Comparisons in the abundances of RNAs isolated from the WT (JMB1100)
1202 and $\Delta fur::tetM$ (JMB1432) strains after culture in TSB medium with and without 120 μM
1203 2,2-dipyridyl (DIP).
1204

1205 **Table S3.** Metabolic modeling simulations corresponding to WT, DIP, Fur, and
1206 FUR_DIP strains using the iYS854 genome-scale metabolic model for *S. aureus* (PMID:
1207 30625152).

1208
1209 **Table S4.** Concentrations of metabolites isolated from the WT (JMB1100) and
1210 $\Delta fur::tetM$ (JMB1432) strains after culture in TSB medium with and without 120 μ M 2,2-
1211 dipyridyl (DIP). The strains were incubated either aerobically or anaerobically in the
1212 absence of a terminal electron acceptor to force fermentative growth. Metabolite
1213 concentrations were standardized by divided them by the optical density of the culture
1214 at the time of harvest.

1215
1216 **Table S5.** List of identified proteins from the YFP-YlaN immunopurifications performed
1217 during logarithmic (LOG) and stationary (STAT) phase growth, with at least 4 identified
1218 peptides in one growth phase and an FDR < 1.0%. The number of unique identified
1219 peptides for each protein are displayed. The MS intensity represents the sum of the
1220 three highest intensity peptides for each protein. Proteins in red text represent those
1221 that bind iron, contain FeS clusters, or are part of the FeS cluster biosynthesis
1222 machinery.

1223

Table 1. Log2 fold-changes of metabolites after aerobic growth*

| WT / WT + 120 μ M DIP | WT / Δfur |
|-----------------------------|--------------------------------|
| <i>Common Metabolites</i> | |
| Pyruvate | -0.5 |
| AICAR (ZMP) | -1.1 |
| Glycine | -1.5 |
| Adenine | -1.1 |
| Guanine | -1.1 |
| Ribulose-5-phosphate | 0.4 |
| Proline | 0.8 |
| Aspartate | 0.8 |
| Serine | -1.9 |
| N-Formyl-L-methionine | 0.4 |
| Succinic acid | -1.0 |
| <i>Unique Metabolites</i> | |
| Acetyl-serine | -2.4 |
| Uracil | -1.0 |
| Thymidine | 0.5 |
| | Cystathionine |
| | Histidine |
| | Argininosuccinate |
| | N-acetyl-L-ornithine |
| | N-acetyl-glutamine |
| | O-Phospho-serine |
| | Glutamine |
| | Citrulline |
| | Arginine |
| | UMP |
| | Guanosine |
| | Adenosine |
| | dTMP |
| | Uridine |
| | GMP |
| | ADP |
| | Thymidine |
| | 2-Deoxyguanosine |
| | IMP |
| | Inosine |
| | Cytidine |
| | O-Succinyl-L-homoserine |
| | Methionine |
| | Methionine sulfoxide |
| | Urocanate |
| | Alanine |
| | Tyrosine |
| | Threonine |
| | Lysine |

| | |
|---------------------|------|
| Tryptophan | -2.0 |
| Phenylalanine | -1.5 |
| Aconitate | -2.8 |
| Alpha-Ketoglutarate | -1.2 |
| Malate | -1.8 |
| Lactate | -0.8 |
| Thymine | -1.1 |
| NAD | -1.3 |
| Mevalonate | -0.8 |
| Pyridoxal | -1.2 |
| Pterine | 1.4 |

***Bold** compounds are increased in a WT strain when compared to the Δfur strain or to WT + DIP.

1225

1226 |

1227

Table 2. Log2 fold-changes of metabolites after anaerobic growth

| WT / WT + 120 μ M DIP | WT / Δfur |
|-----------------------------------|-------------------|
| <i>Common Metabolites</i> | |
| Proline | 0.7 |
| Urocanate | 1.5 |
| Ornithine | 1.0 |
| Histidine | 2.3 |
| Dihydroorotic acid | 2.4 |
| 5-Aminolevulinate | 1.1 |
| <i>Unique Metabolites</i> | |
| Orotate | 0.7 |
| N-carbamoyl-aspartate | 1.0 |
| Asparagine | 0.7 |
| Arginine | 0.4 |
| Pyruvate | -0.4 |
| Phosphoenolpyruvate | 1.2 |
| Glyceraldehyde-3-phosphate | -2.2 |
| Dihydroxyacetone phosphate | -2.4 |
| Deoxycytidine | -0.7 |
| 2-Deoxyguanosine | -2.6 |
| dUMP | -2.0 |
| AMP | 0.5 |
| Pterine | 1.2 |
| NADH | 0.9 |
| Lysine | 0.6 |
| Acetyl-serine | -2.2 |
| Cystine | 1.0 |
| Proline | 1.8 |
| Urocanate | 1.5 |
| Ornithine | 1.1 |
| Histidine | 1.6 |
| Dihydroorotic acid | -2.5 |
| 5-Aminolevulinate | 1.4 |
| N-acetyl-L-ornithine | 0.4 |
| O-Phospho-serine | -2.8 |
| Citrulline | 2.6 |
| Glutamine | 0.7 |
| Argininosuccinate | 3.3 |
| N-acetyl-glutamine | 1.0 |
| 2-Keto-3-deoxy-D-gluconate | 1.3 |
| Diaminopimelic acid | -2.5 |
| Thiamine | -0.5 |
| dUMP | -2.4 |
| CMP | 0.8 |
| AICAR (ZMP) | -1.1 |

***Bold** compounds are increased in a WT strain when compared to the Δfur strain or to WT + DIP.

1228

1229 |

1230

Table 3. Bacterial strains and plasmids used in this study.

***Staphylococcus aureus* USA300_LAC strains**

| Strain name | genotype | Allele reference |
|-------------|------------------------------------|---------------------|
| JMB1100 | USA300_LAC wild type (WT) | Alexander Horswill |
| JMB8689 | $\Delta ylaN::tetM$ | This study |
| JMB8428 | $ylaN::Tn$ | (89) this study |
| JMB1432 | $\Delta fur::tetM$ | (90) |
| JMB4536 | $hemB::Tn$ | (91) |
| JMB10678 | $\Delta ylaN::tetM fur^*$ | This study |
| JMB10675 | $proC::Tn$ | (89) and this study |
| JMB10677 | $\Delta ylaN::tetM proC::Tn$ | (89) and this study |
| JMB10676 | $fur^* proC::Tn$ | (89) and this study |
| JMB10678 | $\Delta ylaN::tetM fur^* proC::Tn$ | (89) and this study |
| JMB7525 | $fhuC::Tn$ | (6) |
| JMB10721 | $\Delta ylaN::tetM fhuC::Tn$ | (89) and this study |
| JMB10722 | $\Delta ylaN::tetM fur^* fhuC::Tn$ | (89) this study |
| JMB10641 | $ylaN::Tn \Delta fur::tetM$ | This study |

***Bacillus subtilis* strains**

| | | |
|--------|--|------------|
| BD630 | <i>hisA1 leuA8 metB5</i> | (92) |
| BD8592 | <i>hisA1 leuA8 metB5 P_{hyperspank} yfp-ylaN</i> | This study |

Plasmids used in this study

| Name | Function | Reference |
|-------------------|---|--------------------|
| pEPSA5 | Inducible expression complementation | (93) |
| pEPSA5_ylaN | Inducible expression complementation | This study |
| pCM28 | Native promoter complementation | (94) |
| pCM28_ylaN | Native promoter complementation | This study |
| pJB38 | Mutant generation | (95) |
| pJB38_ΔylaN::tetM | Mutant generation | This study |
| pDR111-YFP | Protein interaction studies | (96) |
| pED2143 | Protein interaction studies | |
| pOS_saeP_gfp | Transcriptional reporter | Shaun R. Brinsmade |
| pOS_isdC_gfp | Transcriptional reporter | This study |
| pOS_fhuA_gfp | Transcriptional reporter | This study |
| pOS_sbnA_gfp | Transcriptional reporter | This study |
| pOS-1-ptgt | Genetic complementation <i>lgt</i> promoter | (97) |
| pOS-1-ptgt_fur | Genetic complementation <i>lgt</i> promoter | (2) |

1231

1232 **REFERENCES**

1. Imlay JA, Chin SM, Linn S. 1988. Toxic DNA damage by hydrogen peroxide through the Fenton reaction in vivo and in vitro. *Science* 240:640-2.
2. Torres VJ, Attia AS, Mason WJ, Hood MI, Corbin BD, Beasley FC, Anderson KL, Stauff DL, McDonald WH, Zimmerman LJ, Friedman DB, Heinrichs DE, Dunman PM, Skaar EP. 2010. *Staphylococcus aureus* Fur regulates the expression of virulence factors that contribute to the pathogenesis of pneumonia. *Infect Immun* 78:1618-28.
3. Hammer ND, Skaar EP. 2011. Molecular mechanisms of *Staphylococcus aureus* iron acquisition. *Annu Rev Microbiol* 65:129-47.
4. Grim KP, San Francisco B, Radin JN, Brazel EB, Kelliher JL, Parraga Solorzano PK, Kim PC, McDevitt CA, Kehl-Fie TE. 2017. The Metallophore Staphylopine Enables *Staphylococcus aureus* To Compete with the Host for Zinc and Overcome Nutritional Immunity. *mBio* 8.
5. Ghssein G, Brutesco C, Ouerdane L, Fojcik C, Izaute A, Wang S, Hajjar C, Lobinski R, Lemaire D, Richaud P, Voulhoux R, Espaillat A, Cava F, Pignol D, Borezee-Durant E, Arnoux P. 2016. Biosynthesis of a broad-spectrum nicotianamine-like metallophore in *Staphylococcus aureus*. *Science* 352:1105-9.
6. Roberts CA, Al-Tameemi HM, Mashruwala AA, Rosario-Cruz Z, Chauhan U, Sause WE, Torres VJ, Belden WJ, Boyd JM. 2017. The Suf Iron-Sulfur Cluster Biosynthetic System Is Essential in *Staphylococcus aureus*, and Decreased Suf Function Results in Global Metabolic Defects and Reduced Survival in Human Neutrophils. *Infect Immun* 85.
7. Steingard CH, Helmann JD. 2023. Meddling with Metal Sensors: Fur-Family Proteins as Signaling Hubs. *J Bacteriol* 205:e0002223.
8. Price EE, Boyd JM. 2020. Genetic Regulation of Metal Ion Homeostasis in *Staphylococcus aureus*. *Trends Microbiol* 28:821-831.
9. Troxell B, Hassan HM. 2013. Transcriptional regulation by Ferric Uptake Regulator (Fur) in pathogenic bacteria. *Front Cell Infect Microbiol* 3:59.
10. Bagg A, Neilands JB. 1987. Ferric uptake regulation protein acts as a repressor, employing iron (II) as a cofactor to bind the operator of an iron transport operon in *Escherichia coli*. *Biochemistry* 26:5471-7.
11. Escolar L, de Lorenzo V, Perez-Martin J. 1997. Metalloregulation in vitro of the aerobactin promoter of *Escherichia coli* by the Fur (ferric uptake regulation) protein. *Mol Microbiol* 26:799-808.
12. Coronel-Tellez RH, Pospiech M, Barrault M, Liu W, Bordeau V, Vasnier C, Felden B, Sargueil B, Bouloc P. 2022. sRNA-controlled iron sparing response in *Staphylococci*. *Nucleic Acids Res* 50:8529-8546.
13. Peters JM, Colavin A, Shi H, Czarny TL, Larson MH, Wong S, Hawkins JS, Lu CH, Koo BM, Marta E, Shiver AL, Whitehead EH, Weissman JS, Brown ED, Qi LS, Huang KC, Gross CA. 2016. A Comprehensive, CRISPR-based Functional Analysis of Essential Genes in Bacteria. *Cell* 165:1493-506.
14. Rauen U, Springer A, Weisheit D, Petrat F, Korth HG, de Groot H, Sustmann R. 2007. Assessment of chelatable mitochondrial iron by using mitochondrion-selective fluorescent iron indicators with different iron-binding affinities. *Chembiochem* 8:341-52.

1277 15. Yunta F, Garcia-Marco S, Lucena JJ, Gomez-Gallego M, Alcazar R, Sierra MA. 2003.
1278 Chelating agents related to ethylenediamine bis(2-hydroxyphenyl)acetic acid (EDDHA):
1279 synthesis, characterization, and equilibrium studies of the free ligands and their Mg²⁺,
1280 Ca²⁺, Cu²⁺, and Fe³⁺ chelates. *Inorg Chem* 42:5412-21.
1281 16. Bergan T, Klaveness J, Aasen AJ. 2001. Chelating agents. *Cancer Chemotherapy* 47:10-4.
1282 17. Luo Y, Han Z, Chin SM, Linn S. 1994. Three chemically distinct types of oxidants
1283 formed by iron-mediated Fenton reactions in the presence of DNA. *Proc Natl Acad Sci U*
1284 *S A* 91:12438-42.
1285 18. DeGraff W, Hahn SM, Mitchell JB, Krishna MC. 1994. Free radical modes of
1286 cytotoxicity of adriamycin and streptonigrin. *Biochem Pharmacol* 48:1427-35.
1287 19. Mashruwala AA, Pang YY, Rosario-Cruz Z, Chahal HK, Benson MA, Mike LA, Skaar
1288 EP, Torres VJ, Nauseef WM, Boyd JM. 2015. Nfu facilitates the maturation of iron-
1289 sulfur proteins and participates in virulence in *Staphylococcus aureus*. *Mol Microbiol*
1290 95:383-409.
1291 20. Sheldon JR, Heinrichs DE. 2012. The iron-regulated staphylococcal lipoproteins. *Front*
1292 *Cell Infect Microbiol* 2:41.
1293 21. Speziali CD, Dale SE, Henderson JA, Vines ED, Heinrichs DE. 2006. Requirement of
1294 *Staphylococcus aureus* ATP-binding cassette-ATPase FhuC for iron-restricted growth
1295 and evidence that it functions with more than one iron transporter. *J Bacteriol* 188:2048-
1296 55.
1297 22. Hammer ND, Reniere ML, Cassat JE, Zhang Y, Hirsch AO, Indriati Hood M, Skaar EP.
1298 2013. Two heme-dependent terminal oxidases power *Staphylococcus aureus* organ-
1299 specific colonization of the vertebrate host. *MBio* 4.
1300 23. Sims PJ, Waggoner AS, Wang CH, Hoffman JF. 1974. Studies on the mechanism by
1301 which cyanine dyes measure membrane potential in red blood cells and
1302 phosphatidylcholine vesicles. *Biochemistry* 13:3315-30.
1303 24. Bryan LE, Kwan S. 1983. Roles of ribosomal binding, membrane potential, and electron
1304 transport in bacterial uptake of streptomycin and gentamicin. *Antimicrob Agents*
1305 *Chemother* 23:835-45.
1306 25. Seif Y, Monk JM, Mih N, Tsunemoto H, Poudel S, Zuniga C, Broddrick J, Zengler K,
1307 Palsson BO. 2019. A computational knowledge-base elucidates the response of
1308 *Staphylococcus aureus* to different media types. *PLoS Comput Biol* 15:e1006644.
1309 26. Cheung J, Beasley FC, Liu S, Lajoie GA, Heinrichs DE. 2009. Molecular
1310 characterization of staphyloferrin B biosynthesis in *Staphylococcus aureus*. *Mol*
1311 *Microbiol* 74:594-608.
1312 27. Carabetta VJ, Tanner AW, Greco TM, Defrancesco M, Cristea IM, Dubnau D. 2013. A
1313 complex of YlbF, YmcA and YaaT regulates sporulation, competence and biofilm
1314 formation by accelerating the phosphorylation of Spo0A. *Molecular Microbiology*
1315 88:283-300.
1316 28. Rodrigues AV, Kandegedara A, Rotondo JA, Dancis A, Stemmler TL. 2015. Iron loading
1317 site on the Fe-S cluster assembly scaffold protein is distinct from the active site.
1318 *Biometals* 28:567-76.
1319 29. Koebke KJ, Batelu S, Kandegedara A, Smith SR, Stemmler TL. 2020. Refinement of
1320 protein Fe(II) binding characteristics utilizing a competition assay exploiting small
1321 molecule ferrous chelators. *J Inorg Biochem* 203:110882.

1322 30. Dzul SP, Rocha AG, Rawat S, Kandegedara A, Kusowski A, Pain J, Murari A, Pain D,
1323 Dancis A, Stemmler TL. 2017. In vitro characterization of a novel Isu homologue from
1324 *Drosophila melanogaster* for de novo FeS-cluster formation. *Metallomics* 9:48-60.

1325 31. Sreerama N, Woody RW. 2004. Computation and analysis of protein circular dichroism
1326 spectra. *Methods Enzymol* 383:318-51.

1327 32. Bencze KZ, Kondapalli KC, Stemmler TL. 2007. X-Ray Absorption Spectroscopy, p
1328 513-28. In Scott RA, Lukehart CM (ed), *Applications of Physical Methods in Inorganic*
1329 and *Bioinorganic Chemistry: Handbook, Encyclopedia of Inorganic Chemistry*, 2nd
1330 Edition. John Wiley & Sons,LTD, Chichester, UK.

1331 33. Nakano MM, Dailly YP, Zuber P, Clark DP. 1997. Characterization of anaerobic
1332 fermentative growth of *Bacillus subtilis*: identification of fermentation end products and
1333 genes required for growth. *J Bacteriol* 179:6749-55.

1334 34. Cruz Ramos H, Hoffmann T, Marino M, Nedjari H, Presecan-Siedel E, Dreesen O,
1335 Glaser P, Jahn D. 2000. Fermentative metabolism of *Bacillus subtilis*: physiology and
1336 regulation of gene expression. *J Bacteriol* 182:3072-80.

1337 35. Py B, Barras F. 2010. Building Fe-S proteins: bacterial strategies. *Nat Rev Microbiol*
1338 8:436-46.

1339 36. Ledala N, Zhang B, Seravalli J, Powers R, Somerville GA. 2014. Influence of iron and
1340 aeration on *Staphylococcus aureus* growth, metabolism, and transcription. *J Bacteriol*
1341 196:2178-89.

1342 37. Friedman DB, Stauff DL, Pishchany G, Whitwell CW, Torres VJ, Skaar EP. 2006.
1343 *Staphylococcus aureus* redirects central metabolism to increase iron availability. *PLoS*
1344 Pathog 2:e87.

1345 38. Nunoshiba T, Obata F, Boss AC, Oikawa S, Mori T, Kawanishi S, Yamamoto K. 1999.
1346 Role of iron and superoxide for generation of hydroxyl radical, oxidative DNA lesions,
1347 and mutagenesis in *Escherichia coli*. *J Biol Chem* 274:34832-7.

1348 39. L. D. R. B. K. S. B. H. R. W. J. R. J. S. 2023. Control of iron homeostasis by a regulatory
1349 protein-protein interaction in *Bacillus subtilis*: The FurA (YlaN) acts as an antirepressor
1350 to the ferric uptake regulator Fur. in review.

1351 40. Bou-Abdallah F, Adinolfi S, Pastore A, Laue TM, Dennis Chasteen N. 2004. Iron
1352 binding and oxidation kinetics in frataxin CyaY of *Escherichia coli*. *Journal of Molecular*
1353 *Biology* 341:605-615.

1354 41. Pastore C, Adinolfi S, Huynen MA, Rybin V, Martin S, Mayer M, Bukau B, Pastore A.
1355 2006. YfhJ, a molecular adaptor in iron-sulfur cluster formation or a frataxin-like
1356 protein? *Structure* 14:857-67.

1357 42. Roche B, Huguenot A, Barras F, Py B. 2015. The iron-binding CyaY and IscX proteins
1358 assist the ISC-catalyzed Fe-S biogenesis in *Escherichia coli*. *Mol Microbiol* 95:605-23.

1359 43. Pang YY, Schwartz J, Bloomberg S, Boyd JM, Horswill AR, Nauseef WM. 2013.
1360 Methionine Sulfoxide Reductases Protect against Oxidative Stress in *Staphylococcus*
1361 *aureus* Encountering Exogenous Oxidants and Human Neutrophils. *J Innate Immun*
1362 doi:10.1159/000355915.

1363 44. Al-Tameemi H, Beavers WN, Norambuena J, Skaar EP, Boyd JM. 2021. *Staphylococcus*
1364 *aureus* lacking a functional MntABC manganese import system has increased resistance
1365 to copper. *Mol Microbiol* 115:554-573.

1366 45. Kreiswirth BN, Löfdahl S, Betley MJ, O'Reilly M, Schlievert PM, Bergdoll MS, Novick
1367 RP. 1983. The toxic shock syndrome exotoxin structural gene is not detectably
1368 transmitted by a prophage. *Nature* 305:709-712.

1369 46. Novick RP. 1991. [27] Genetic systems in Staphylococci, p 587-636, *Methods in*
1370 *Enzymology*, vol 204. Academic Press.

1371 47. Rosario-Cruz Z, Chahal HK, Mike LA, Skaar EP, Boyd JM. 2015. Bacillithiol has a role
1372 in Fe-S cluster biogenesis in *Staphylococcus aureus*. *Mol Microbiol* 98:218-42.

1373 48. Mashruwala AA, Boyd JM. 2015. De Novo Assembly of Plasmids Using Yeast
1374 Recombinational Cloning. *Methods Mol Biol* 1373:33-41.

1375 49. Joska TM, Mashruwala A, Boyd JM, Belden WJ. 2014. A universal cloning method
1376 based on yeast homologous recombination that is simple, efficient, and versatile. *J*
1377 *Microbiol Methods* 100:46-51.

1378 50. Mashruwala AA, Bhatt S, Poudel S, Boyd ES, Boyd JM. 2016. The DUF59 Containing
1379 Protein SuFT Is Involved in the Maturation of Iron-Sulfur (FeS) Proteins during
1380 Conditions of High FeS Cofactor Demand in *Staphylococcus aureus*. *PLoS Genet*
1381 12:e1006233.

1382 51. Olson BJ, Markwell J. 2007. Assays for determination of protein concentration. *Curr*
1383 *Protoc Protein Sci Chapter 3:Unit 3 4.*

1384 52. Carroll RK, Weiss A, Shaw LN. 2016. RNA-Sequencing of *Staphylococcus aureus*
1385 Messenger RNA. *Methods Mol Biol* 1373:131-41.

1386 53. Carroll RK, Weiss A, Broach WH, Wiemels RE, Mogen AB, Rice KC, Shaw LN. 2016.
1387 Genome-wide Annotation, Identification, and Global Transcriptomic Analysis of
1388 Regulatory or Small RNA Gene Expression in *Staphylococcus aureus*. *mBio* 7:e01990-
1389 15.

1390 54. Tatusov RL, Galperin MY, Natale DA, Koonin EV. 2000. The COG database: a tool for
1391 genome-scale analysis of protein functions and evolution. *Nucleic Acids Res* 28:33-6.

1392 55. Bastock RA, Marino EC, Wiemels RE, Holzschu DL, Keogh RA, Zapf RL, Murphy ER,
1393 Carroll RK. 2021. *Staphylococcus aureus* Responds to Physiologically Relevant
1394 Temperature Changes by Altering Its Global Transcript and Protein Profile. *mSphere* 6.

1395 56. Schmittgen TD, Livak KJ. 2008. Analyzing real-time PCR data by the comparative C(T)
1396 method. *Nat Protoc* 3:1101-8.

1397 57. Yang JH, Wright SN, Hamblin M, McCloskey D, Alcantar MA, Schrubbers L, Lopatkin
1398 AJ, Satish S, Nili A, Palsson BO, Walker GC, Collins JJ. 2019. A White-Box Machine
1399 Learning Approach for Revealing Antibiotic Mechanisms of Action. *Cell* 177:1649-1661
1400 e9.

1401 58. Shlomi T, Cabili MN, Herrgard MJ, Palsson BO, Ruppin E. 2008. Network-based
1402 prediction of human tissue-specific metabolism. *Nat Biotechnol* 26:1003-10.

1403 59. Zur H, Ruppin E, Shlomi T. 2010. iMAT: an integrative metabolic analysis tool.
1404 *Bioinformatics* 26:3140-2.

1405 60. Ebrahim A, Lerman JA, Palsson BO, Hyduke DR. 2013. COBRApy: COnstraints-Based
1406 Reconstruction and Analysis for Python. *BMC Syst Biol* 7:74.

1407 61. Megchelenbrink W, Huynen M, Marchiori E. 2014. optGpSampler: an improved tool for
1408 uniformly sampling the solution-space of genome-scale metabolic networks. *PLoS One*
1409 9:e86587.

1410 62. Patel JS, Norambuena J, Al-Tameemi H, Ahn YM, Perryman AL, Wang X, Daher SS,
1411 Occi J, Russo R, Park S, Zimmerman M, Ho HP, Perlin DS, Dartois V, Ekins S, Kumar

1412 P, Connell N, Boyd JM, Freundlich JS. 2021. Bayesian Modeling and Intrabacterial Drug
1413 Metabolism Applied to Drug-Resistant *Staphylococcus aureus*. *ACS Infect Dis* 7:2508-
1414 2521.

1415 63. Melamud E, Vastag L, Rabinowitz JD. 2010. Metabolomic analysis and visualization
1416 engine for LC-MS data. *Anal Chem* 82:9818-26.

1417 64. Schwyn B, Neilands JB. 1987. Universal chemical assay for the detection and
1418 determination of siderophores. *Anal Biochem* 160:47-56.

1419 65. Arora NK, Verma M. 2017. Modified microplate method for rapid and efficient
1420 estimation of siderophore produced by bacteria. *3 Biotech* 7:381.

1421 66. Buchfink B, Reuter K, Drost HG. 2021. Sensitive protein alignments at tree-of-life scale
1422 using DIAMOND. *Nat Methods* 18:366-368.

1423 67. Katoh K, Kuma K, Toh H, Miyata T. 2005. MAFFT version 5: improvement in accuracy
1424 of multiple sequence alignment. *Nucleic Acids Res* 33:511-8.

1425 68. Lefort V, Desper R, Gascuel O. 2015. FastME 2.0: A Comprehensive, Accurate, and Fast
1426 Distance-Based Phylogeny Inference Program. *Mol Biol Evol* 32:2798-800.

1427 69. Lemoine F, Gascuel O. 2021. Gotree/Goalign: toolkit and Go API to facilitate the
1428 development of phylogenetic workflows. *NAR Genom Bioinform* 3:1qab075.

1429 70. Letunic I, Bork P. 2021. Interactive Tree Of Life (iTOL) v5: an online tool for
1430 phylogenetic tree display and annotation. *Nucleic Acids Res* 49:W293-W296.

1431 71. Galili T. 2015. dendextend: an R package for visualizing, adjusting and comparing trees
1432 of hierarchical clustering. *Bioinformatics* 31:3718-20.

1433 72. Moriya Y, Itoh M, Okuda S, Yoshizawa AC, Kanehisa M. 2007. KAAS: an automatic
1434 genome annotation and pathway reconstruction server. *Nucleic Acids Res* 35:W182-5.

1435 73. Jumper J, Evans R, Pritzel A, Green T, Figurnov M, Ronneberger O, Tunyasuvunakool
1436 K, Bates R, Zidek A, Potapenko A, Bridgland A, Meyer C, Kohl SAA, Ballard AJ,
1437 Cowie A, Romera-Paredes B, Nikolov S, Jain R, Adler J, Back T, Petersen S, Reiman D,
1438 Clancy E, Zielinski M, Steinegger M, Pacholska M, Berghammer T, Bodenstein S, Silver
1439 D, Vinyals O, Senior AW, Kavukcuoglu K, Kohli P, Hassabis D. 2021. Highly accurate
1440 protein structure prediction with AlphaFold. *Nature* 596:583-589.

1441 74. Greco TM, Miteva Y, Conlon FL, Cristea IM. 2012. Complementary proteomic analysis
1442 of protein complexes. *Methods Mol Biol* 917:391-407.

1443 75. Tsai YC, Greco TM, Boonmee A, Miteva Y, Cristea IM. 2012. Functional proteomics
1444 establishes the interaction of SIRT7 with chromatin remodeling complexes and expands
1445 its role in regulation of RNA polymerase I transcription. *Mol Cell Proteomics*
1446 11:M111.015156.

1447 76. Wiśniewski JR, Zougman A, Nagaraj N, Mann M. 2009. Universal sample preparation
1448 method for proteome analysis. *Nat Methods* 6:359-62.

1449 77. Manza LL, Stamer SL, Ham AJ, Codreanu SG, Liebler DC. 2005. Sample preparation
1450 and digestion for proteomic analyses using spin filters. *Proteomics* 5:1742-5.

1451 78. Erde J, Loo RR, Loo JA. 2014. Enhanced FASP (eFASP) to increase proteome coverage
1452 and sample recovery for quantitative proteomic experiments. *J Proteome Res* 13:1885-95.

1453 79. Carabetta VJ, Greco TM, Cristea IM, Dubnau D. 2019. YfmK is an Ne-lysine
1454 acetyltransferase that directly acetylates the histone-like protein HBsu in *Bacillus subtilis*.
1455 *Proceedings of the National Academy of Sciences* 116:3752-3757.

1456 80. Masuda T, Tomita M, Ishihama Y. 2008. Phase transfer surfactant-aided trypsin digestion
1457 for membrane proteome analysis. *Journal of Proteome Research* 7:731-740.

1458 81. Kulak NA, Pichler G, Paron I, Nagaraj N, Mann M. 2014. Minimal, encapsulated
1459 proteomic-sample processing applied to copy-number estimation in eukaryotic cells.
1460 *Nature Methods* 11:319-324.

1461 82. Ashford P, Hernandez A, Greco TM, Buch A, Sodeik B, Cristea IM, Grünewald K,
1462 Shepherd A, Topf M. 2016. HVint: A strategy for identifying novel protein-protein
1463 interactions in Herpes Simplex Virus Type 1. *Mol Cell Proteomics* 15:2939-53.

1464 83. Grossmann J, Roschitzki B, Panse C, Fortes C, Barkow-Oesterreicher S, Rutishauser D,
1465 Schlapbach R. 2010. Implementation and evaluation of relative and absolute
1466 quantification in shotgun proteomics with label-free methods. *J Proteomics* 73:1740-6.

1467 84. Kuzmić P. 1996. Program DYNAFIT for the Analysis of Enzyme Kinetic Data:
1468 Application to HIV Proteinase. *Analytical Biochemistry* 237:260-273.

1469 85. George GN, George SJ, Pickering IJ. 2001. EXAFSPAK, <http://www-ssrl.slac.stanford.edu/~george/exafspak/exafs.htm>, Menlo Park, CA.

1470 86. Ankudinov AL, Rehr JJ. 1997. Relativistic Spin-dependent X-ray Absorption Theory.
1471 *Phys Rev B* 56:1712.

1472 87. Cook JD, Kondapalli KC, Rawat S, Childs WC, Murugesan Y, Dancis A, Stemmler TL.
1473 2010. Molecular details of the yeast frataxin-Isu1 interaction during mitochondrial Fe-S
1474 cluster assembly. *Biochemistry* 49:8756-65.

1475 88. Riggs-Gelasco PJ, Stemmler TL, Penner-Hahn JE. 1995. XAFS of Dinuclear Metal Sites
1476 in Proteins and Model Compounds. *Coord Chem Review* 114.

1477 89. Fey PD, Endres JL, Yajjala VK, Widhalm TJ, Boissy RJ, Bose JL, Bayles KW. 2013. A
1478 genetic resource for rapid and comprehensive phenotype screening of nonessential
1479 *Staphylococcus aureus* genes. *MBio* 4:e00537-12.

1480 90. Mashruwala AA, Roberts CA, Bhatt S, May KL, Carroll RK, Shaw LN, Boyd JM. 2016.
1481 *Staphylococcus aureus* SufT: An essential iron-sulfur cluster assembly factor in cells
1482 experiencing a high-demand for lipoic acid. *Mol Microbiol* doi:10.1111/mmi.13539.

1483 91. Mashruwala AA, Van De Guchte A, Boyd JM. 2017. Impaired respiration elicits SrrAB-
1484 dependent programmed cell lysis and biofilm formation in *Staphylococcus aureus*. *eLife*
1485 6.

1486 92. Albano M, Hahn J, Dubnau D. 1987. Expression of competence genes in *Bacillus*
1487 *subtilis*. *J Bacteriol* 169:3110-7.

1488 93. Forsyth RA, Haselbeck RJ, Ohlsen KL, Yamamoto RT, Xu H, Trawick JD, Wall D,
1489 Wang L, Brown-Driver V, Froelich JM, C KG, King P, McCarthy M, Malone C, Misiner
1490 B, Robbins D, Tan Z, Zhu Zy ZY, Carr G, Mosca DA, Zamudio C, Foulkes JG, Zyskind
1491 JW. 2002. A genome-wide strategy for the identification of essential genes in
1492 *Staphylococcus aureus*. *Mol Microbiol* 43:1387-400.

1493 94. Pang YY, Schwartz J, Thoendel M, Ackermann LW, Horswill AR, Nauseef WM. agr-
1494 Dependent interactions of *Staphylococcus aureus* USA300 with human
1495 polymorphonuclear neutrophils. *J Innate Immun* 2:546-59.

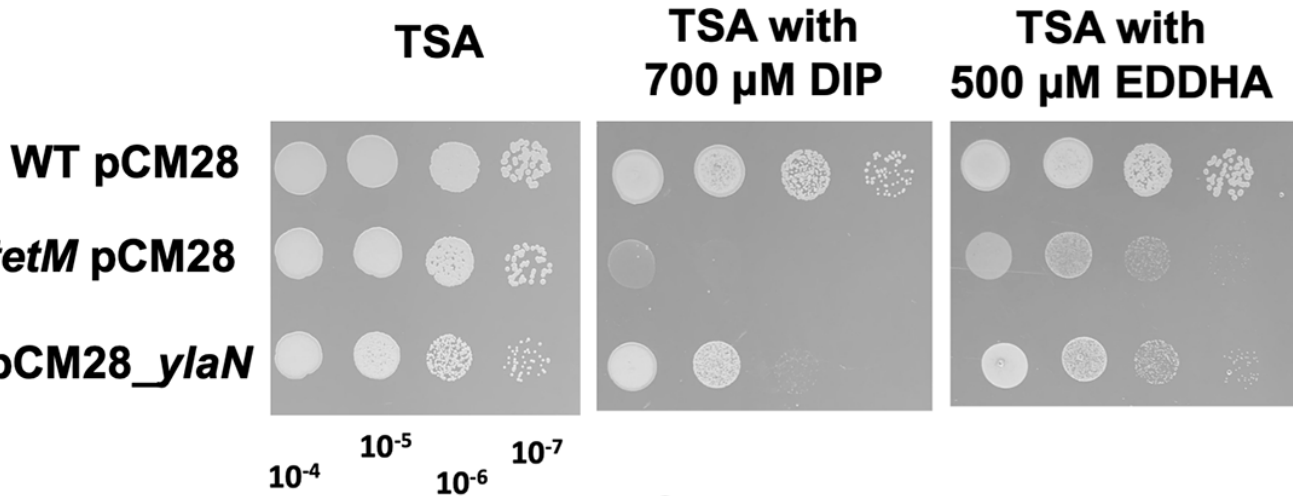
1496 95. Bose JL, Fey PD, Bayles KW. 2013. Genetic tools to enhance the study of gene function
1497 and regulation in *Staphylococcus aureus*. *Appl Environ Microbiol* 79:2218-24.

1498 96. Kramer N, Hahn J, Dubnau D. 2007. Multiple interactions among the competence
1499 proteins of *Bacillus subtilis*. *Mol Microbiol* 65:454-64.

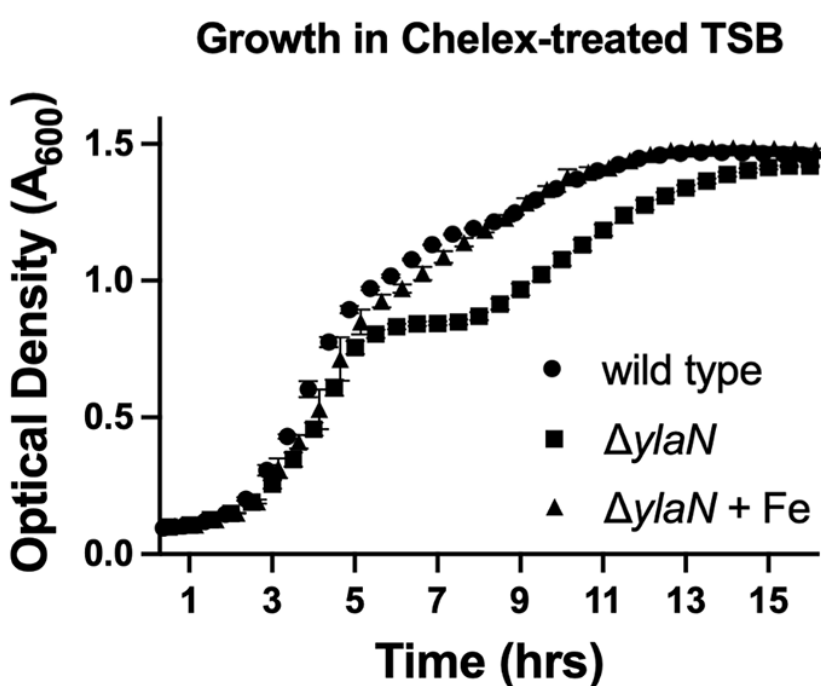
1500 97. Bubeck Wardenburg J, Williams WA, Missiakas D. 2006. Host defenses against
1501 *Staphylococcus aureus* infection require recognition of bacterial lipoproteins. *Proc Natl
1502 Acad Sci U S A* 103:13831-6.

1503

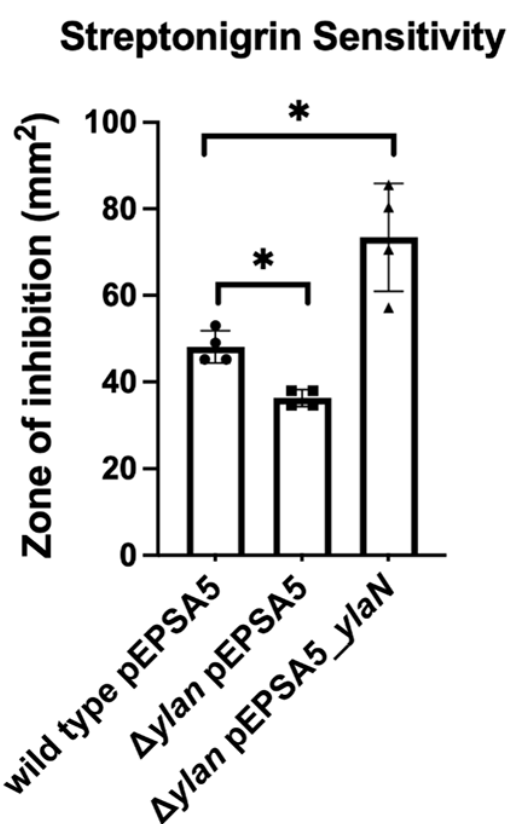
A



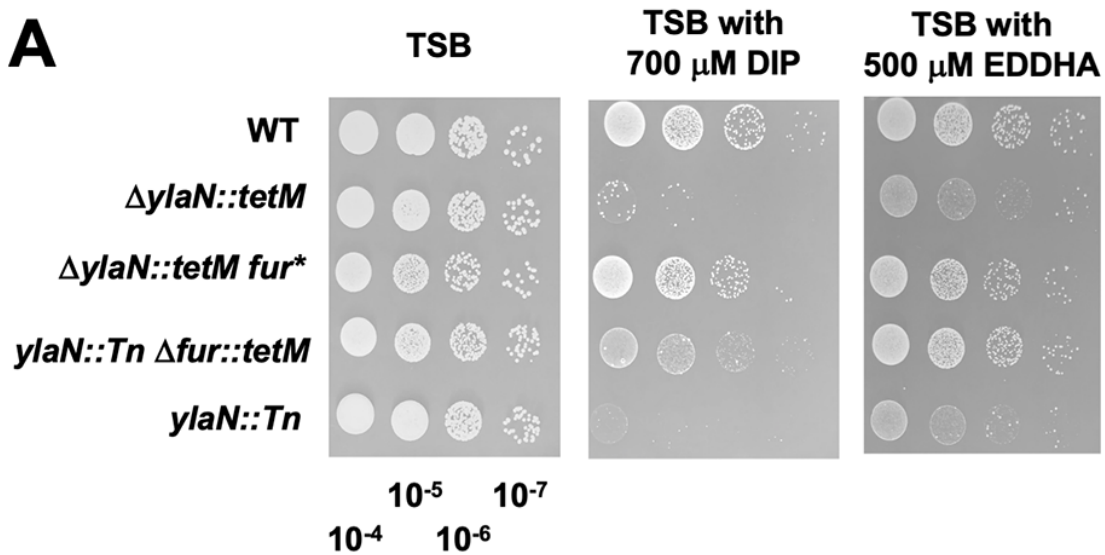
B



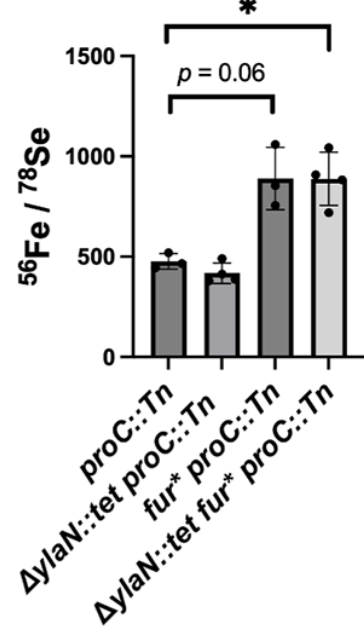
C



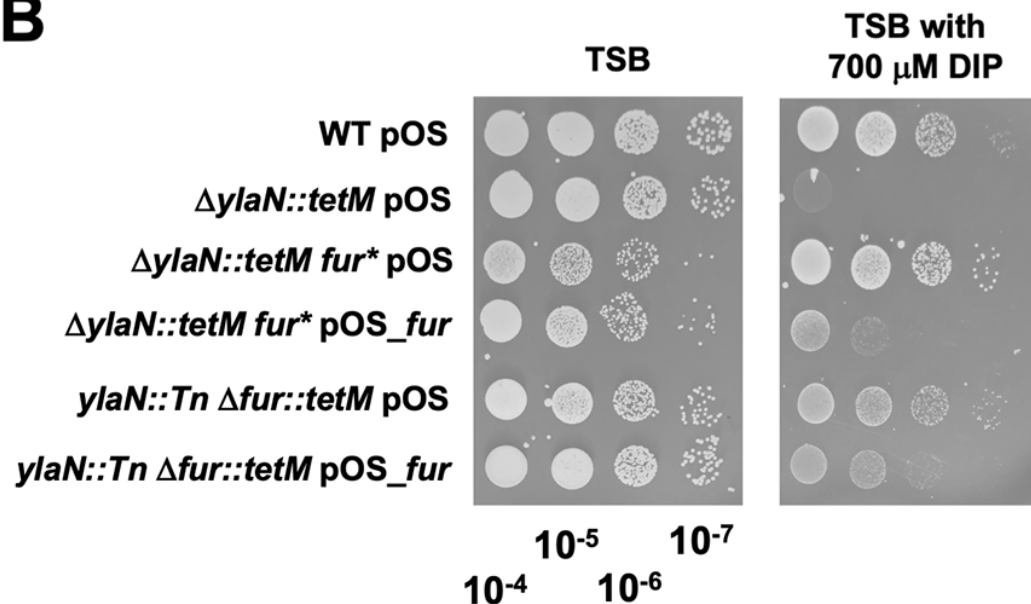
A



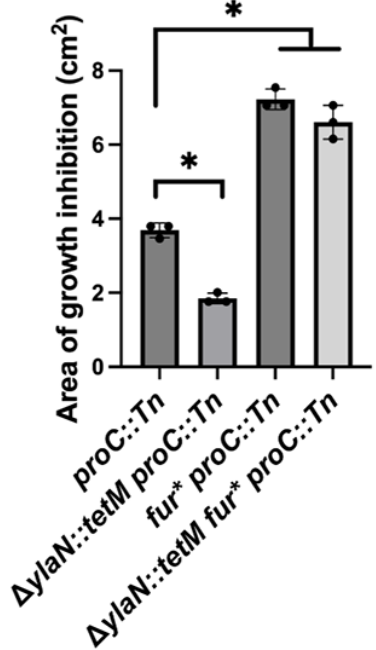
C Cellular Fe Content

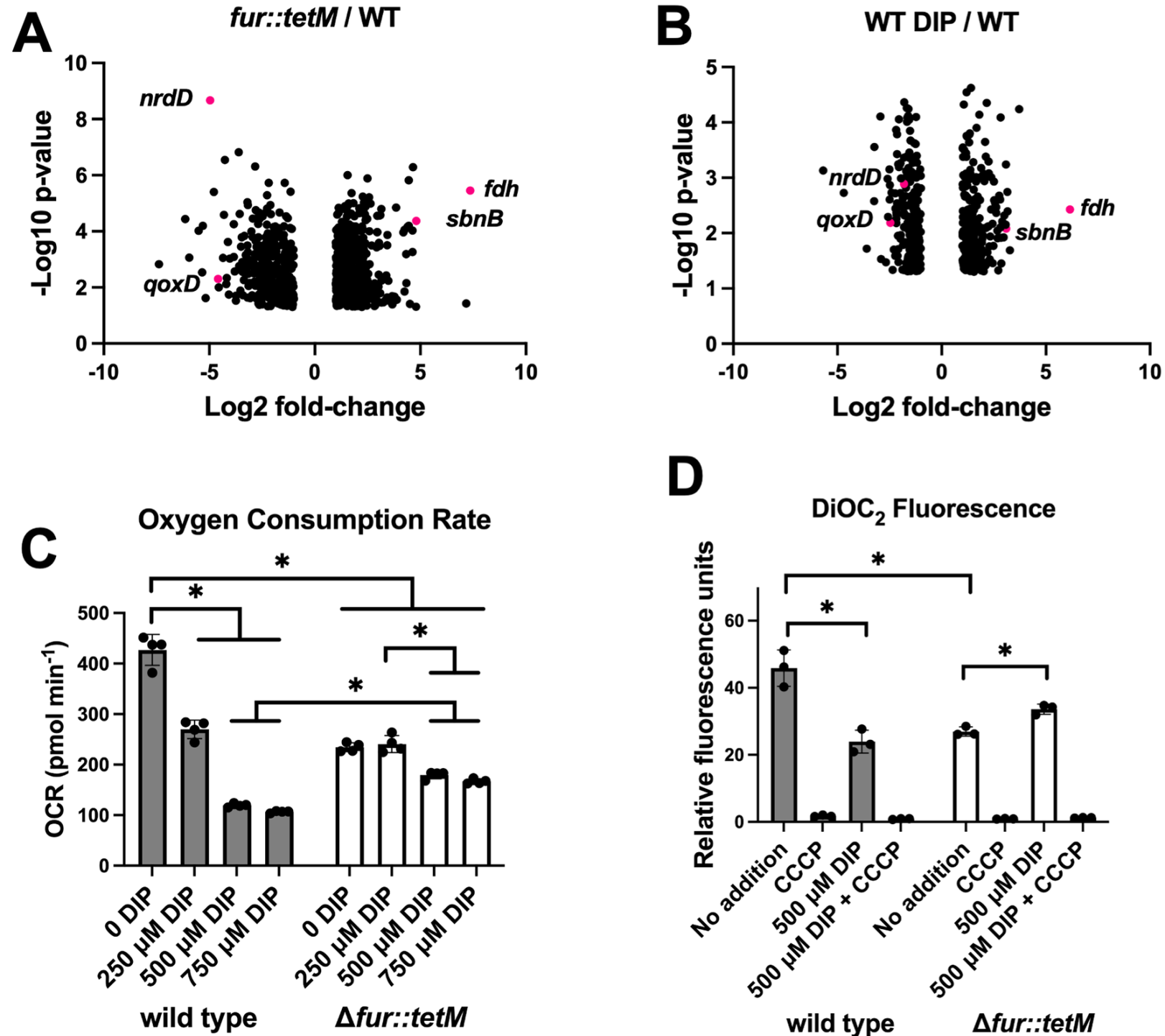


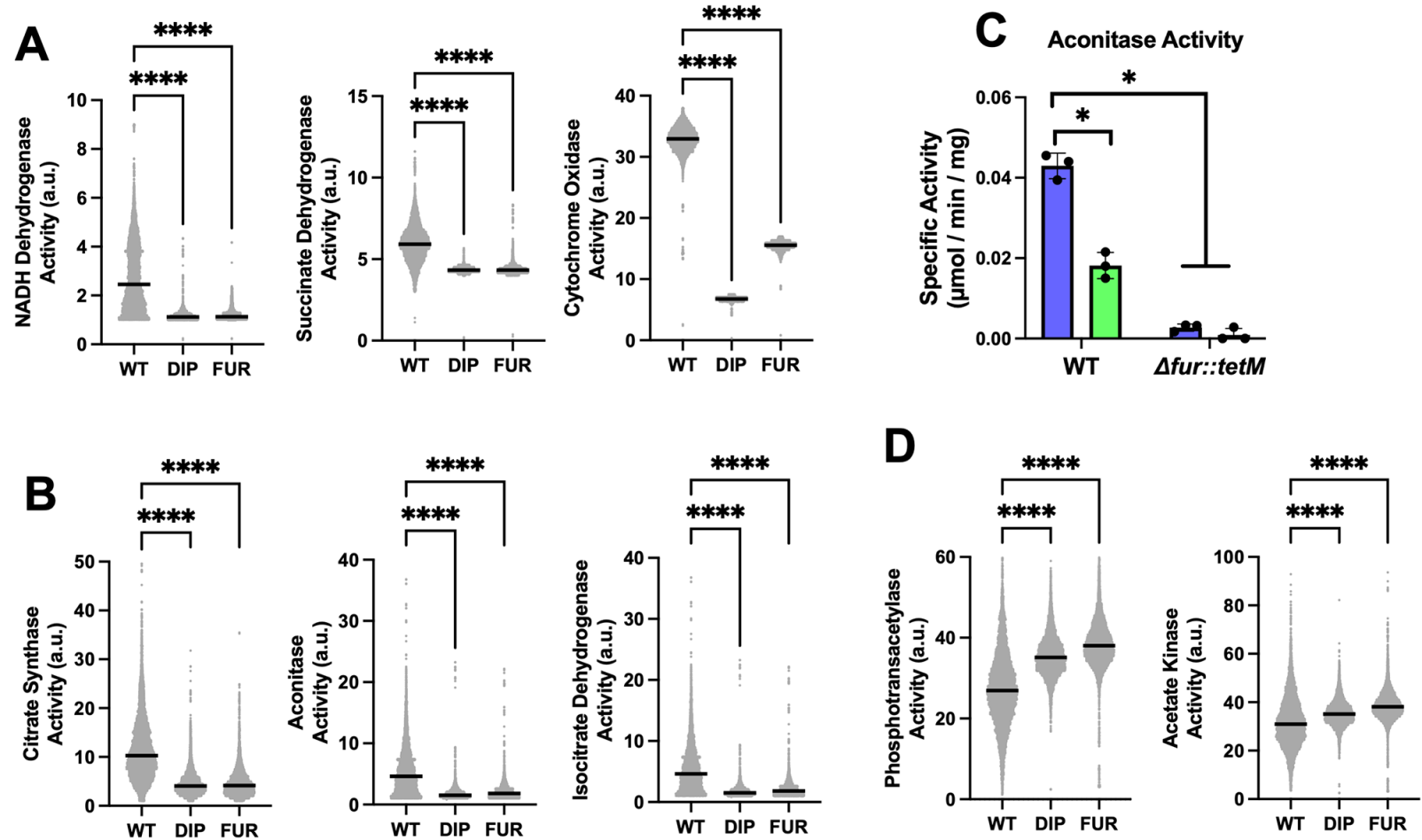
B

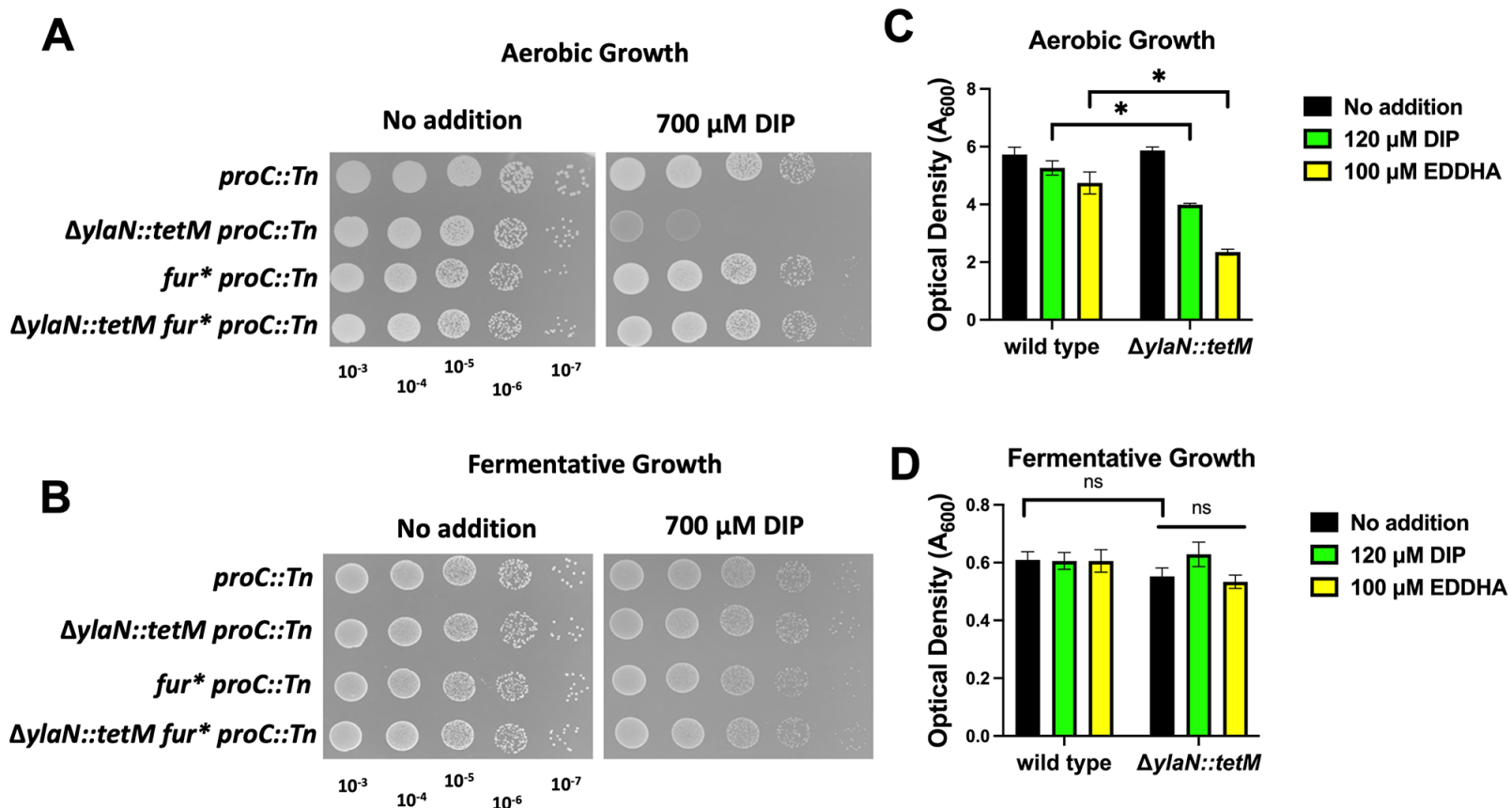


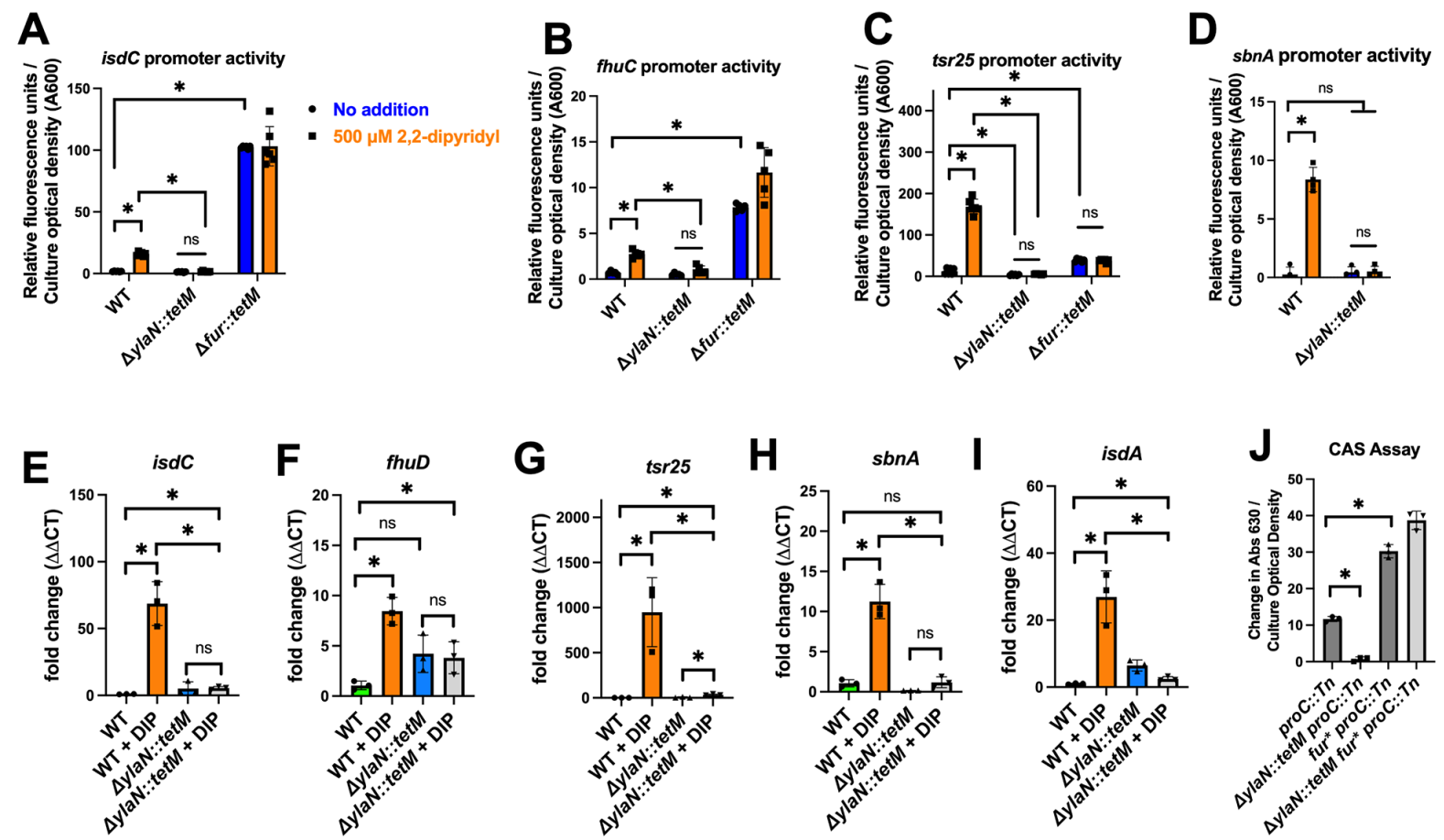
D Streptonigrin Sensitivity

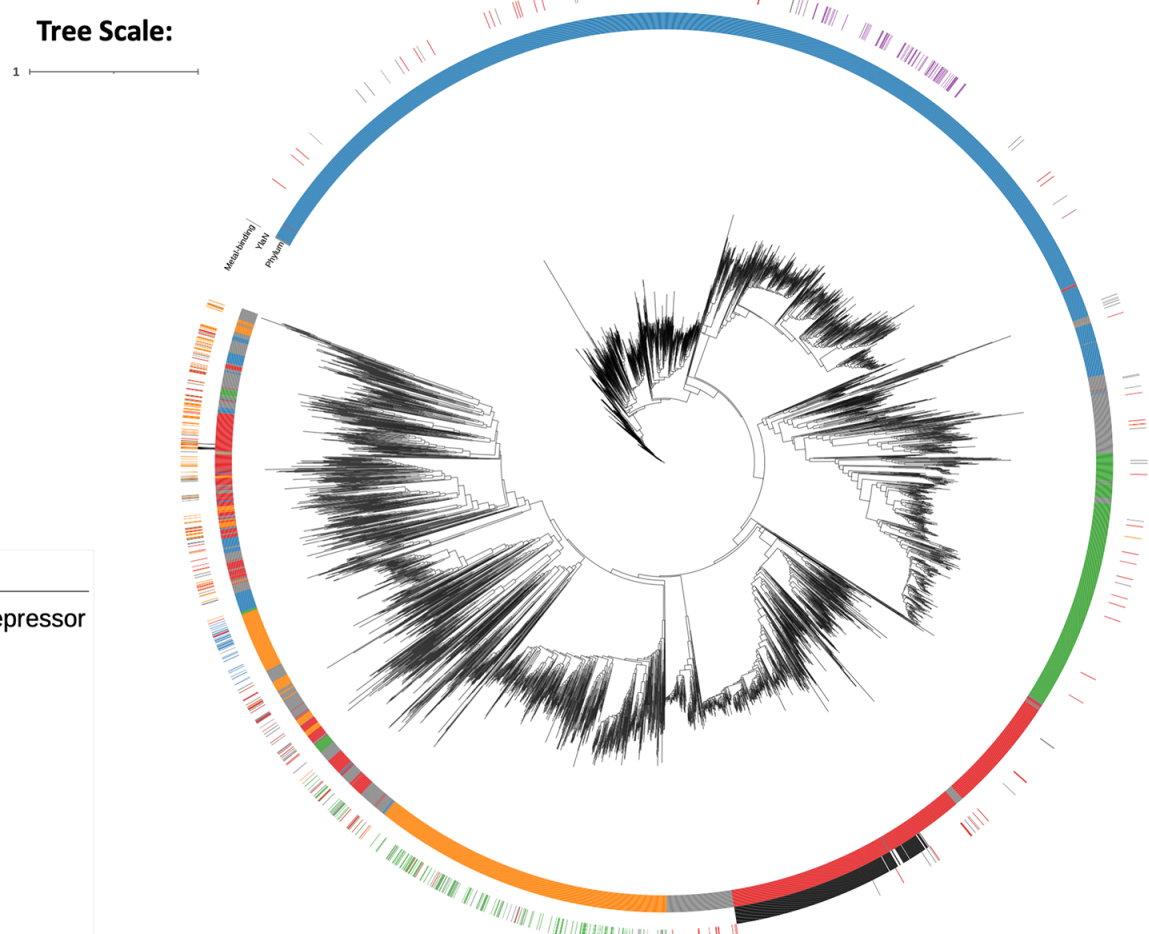
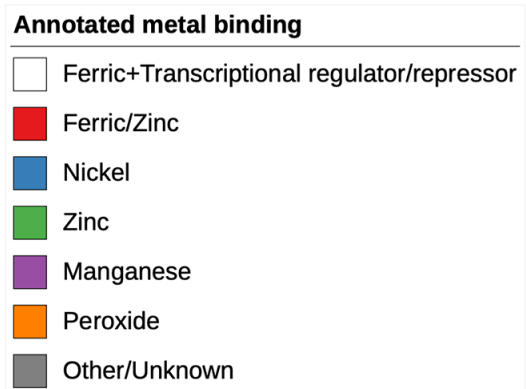
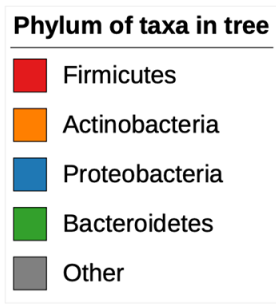


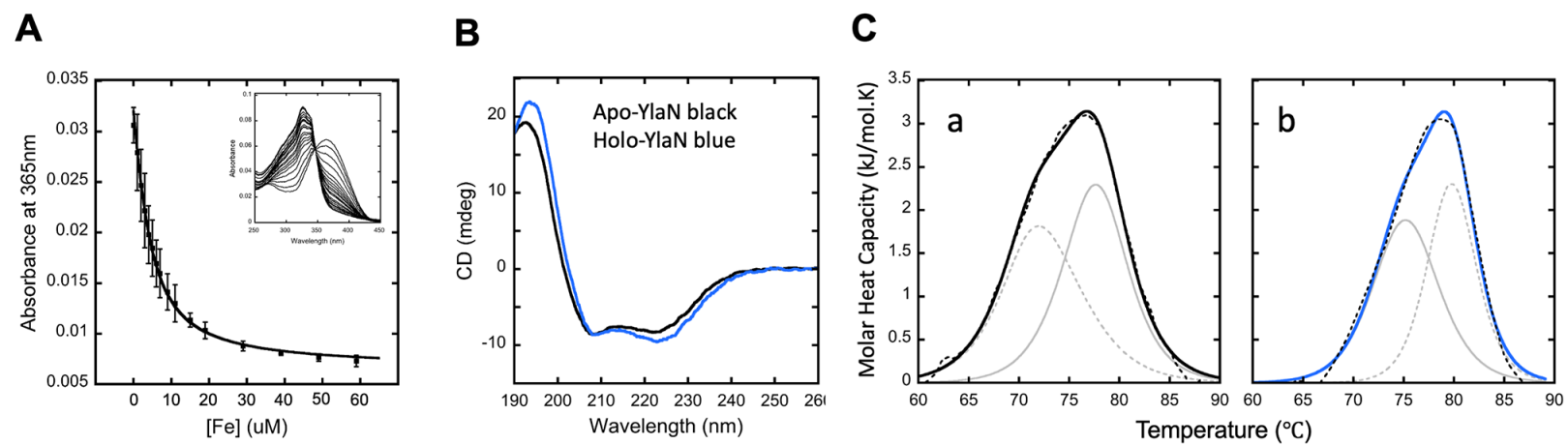


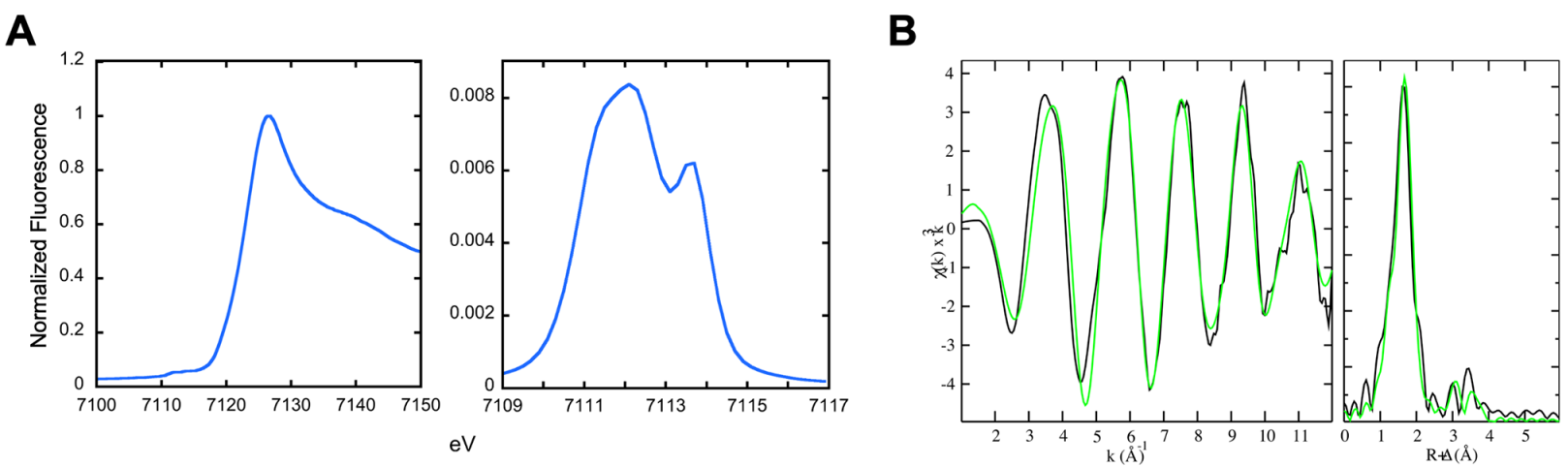




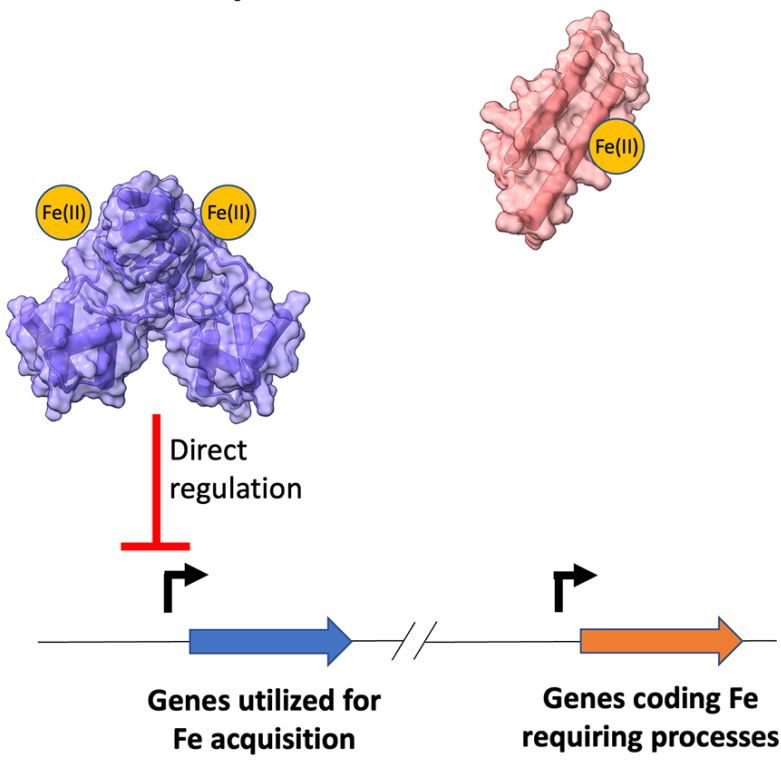








Fe replete conditions



Fe deplete conditions

